A&A, 710, A281 (2026)
https://doi.org/10.1051/0004-6361/202558798

Astronomy & Astrophysics

Exploring the conditions for forming planetesimals via the streaming instability and planetary systems via pebble accretion

Anders Johansen[1,2,⋆] and Wladimir Lyra[3]

[1] Center for Star and Planet Formation, Globe Institute, University of Copenhagen, Øster Voldgade 5-7, 1350 Copenhagen, Denmark
[2] Division of Astrophysics, Department of Physics, Lund University, Box 118, 22100 Lund, Sweden
[3] New Mexico State University, Department of Astronomy, PO Box 30001 MSC 4500, Las Cruces, NM 88001, USA

Received 26 December 2025 / Accepted 28 April 2026

ABSTRACT

The streaming instability and pebble accretion are two physical mechanisms with demonstrated potentials to drive, respectively, the formation of planetesimals and the growth of planetary systems containing a diverse range of planetary types. Here we explore the protoplanetary disc conditions in terms of turbulence strength, Stokes number, and initial disc size that are needed to (i) form planetesimals by the streaming instability, (ii) form gas giant planets in cold orbits, (iii) form super-Earths and sub-Neptunes close to the star, and (iv) form rocky planet embryos in temperate orbits. We identify an optimum Stokes number range between St = 0.01 and St = 0.03 where all three planetary classes form and where the streaming instability is triggered for a slightly elevated pebble metallicity. Cold gas giants require a turbulence strength of at most $\delta = 10^{-4}$ and furthermore need large initial disc sizes to benefit from a prolonged pebble flux; super-Earths and rocky planet embryos tolerate higher turbulence strengths similar to those measured for the vertical shear instability. A higher Stokes number of St = 0.1 is detrimental to the formation of cold gas giants due to the short-lived pebble flux. For Stokes numbers below St = 0.003, extremely low values of turbulence ($\delta < 10^{-5}$) are required to form cold gas giants. We highlight how loss of gas to disc winds, reduction in the migration speed by thermal or dynamical torques, or the presence of pressure bumps in the outer disc could increase the parameter space for the formation of cold gas giants. We derive analytically that the mass of the largest planetesimals formed by the streaming instability is of similar magnitude to the threshold mass beyond which pebble accretion becomes efficient, if planetesimals form in the earliest phases of protoplanetary disc evolution.

Key words. planets and satellites: composition – planets and satellites: formation – planets and satellites: gaseous planets – planets and satellites: terrestrial planets – planet-disk interactions

1. Introduction

The dense environment of a protoplanetary disc facilitates collisional sticking of micrometre-sized particles consisting of silicate rock and metal as well as volatile ices. Collisions driven by turbulence become ever faster as the dust aggregates grow to larger sizes, until the collision speed reaches the threshold above which the internal rearrangement of monomers can no longer absorb the collision energy (Dullemond & Dominik 2005; Brauer et al. 2008), so that the collision leads to fragmentation rather than sticking. The fragmentation threshold speed for silicate dust aggregates is generally found to lie at approximately 1 m/s (Güttler et al. 2010), but its value may increase to 5–10 m/s at the high temperatures in the innermost regions of the protoplanetary disc, due to the higher surface energy of dry silicates at elevated temperatures (Kimura et al. 2015).

The sticking threshold of water ice has been measured to be very high, of the order of 10 m/s (Gundlach & Blum 2015). Experiments under realistic temperature conditions, applicable in the icy regions of the protoplanetary disc (temperature $T < 170\,\mathrm{K}$), nevertheless show a dramatic drop in surface energy (Gundlach et al. 2018) and imply a fragmentation threshold speed for water ice that is similar to that of silicates (Musiolik & Wurm 2019). Even more volatile CO_2 ice has also been experimentally tested to have a sticking threshold similar to that of silicates (Musiolik et al. 2016; Fritscher & Teiser 2021).

Reaching the fragmentation barrier requires that the aggregates remain porous during their growth since compact particles experience bouncing already at much lower collision speeds (Zsom et al. 2010; Arakawa et al. 2023; Dominik & Dullemond 2024; Qian & Wu 2025). In addition, if monomers are smaller than the usually assumed 1 µm, this would lead to higher fragmentation thresholds (Okuzumi et al. 2012). The fragmentation barrier (Birnstiel et al. 2011), despite its simplifications in terms of ignoring porosity evolution, has nevertheless emerged as a useful reference point for understanding growth from dust to pebbles in protoplanetary discs (Jiang et al. 2024; Tong et al. 2026). The Stokes number St of pebbles at the fragmentation barrier is found by equating the threshold speed for fragmentation, v_f, with the turbulent collision speed, $v_\mathrm{t} = \sqrt{3\mathrm{St}\,\delta}c_\mathrm{s}$, to obtain

$$\mathrm{St} = \frac{1}{3}\frac{1}{\delta}\left(\frac{v_\mathrm{f}}{c_\mathrm{s}}\right)^2 \approx 0.01\left(\frac{\delta}{10^{-4}}\right)^{-1}\left(\frac{T}{100\,\mathrm{K}}\right)^{-1}\left(\frac{v_\mathrm{f}}{1\,\mathrm{m/s}}\right)^2. \quad (1)$$

Here, δ is a dimensionless measure of the strength of the turbulence (related to the turbulent diffusion coefficient D through the scaling $D = \delta c_\mathrm{s} H$, where c_s is the gas sound speed and H is the gas scale-height). A fragmentation threshold of $v_\mathrm{f} \sim 1$ m/s and a turbulence strength $\delta \sim 10^{-4}$ are found to be in good agreement with the millimetre–centimetre wavelength emission

⋆ Corresponding author: Anders.Johansen@sund.ku.dk

from pebbles in a range of observed protoplanetary discs (Jiang et al. 2024; Tong et al. 2026) and indicates a nominal Stokes number of order St∼0.01. Extraction of the pebble Stokes number from protoplanetary disc observations nevertheless comes with a large uncertainty, due to among other things the assumed opacity of the pebbles and their poorly constrained porosity (Ueda et al. 2025).

The realization that particle growth in protoplanetary discs likely stalls at pebble sizes – historically achieved from a combination of dust collision experiments (Blum & Wurm 2000), computer simulations of dust coagulation including fragmentation and radial drift (Dullemond & Dominik 2005), and observations of emission from pebbles in protoplanetary discs at millimetre–centimetre wavelengths (Testi et al. 2003; Wilner et al. 2005) – inspired the development of the streaming instability theory for planetesimal formation (Youdin & Goodman 2005; Youdin & Johansen 2007; Johansen & Youdin 2007). Through the action of the streaming instability, radially drifting pebbles will spontaneously gather into dense filaments, due to their drag force interaction with the background gas, forming 100 km-scale planetesimals from the gravitational contraction of the filaments (Johansen et al. 2007, 2015; Simon et al. 2016). However, the threshold metallicity, defined as the local pebble surface density relative to the gas surface density, needed for triggering the emergence of dense filaments depends both on the pebble Stokes number and the strength of the background turbulence (Carrera et al. 2015; Yang et al. 2017; Li & Youdin 2021; Lim et al. 2024).

The presence of planetesimals, leftovers from the formation epoch of our Solar System, in the asteroid belt between Mars and Jupiter inspired the planetesimal-driven model of planet formation (Safronov 1969). A combination of planetesimal accretion and giant impacts between protoplanets can broadly explain the formation of planets similar to Earth and Venus in mass over a timescale of ∼100 million years (Chambers & Wetherill 1998; Kokubo & Ida 2000; Raymond et al. 2004), and the role of giant impacts in the growth of terrestrial planets is supported by the need for the Earth to undergo at least one impact in order to explain the mantle-like bulk composition of the moon (Kokubo & Ida 2007).

In contrast, the accumulation timescale of 100 km-scale planetesimals in the outer Solar System, where gas giants and ice giants form, takes much longer than the lifetime of the protoplanetary disc (Thommes et al. 2003; Levison et al. 2010; Johansen & Bitsch 2019; Lorek & Johansen 2022; Kaufmann et al. 2025). Considering much smaller planetesimals (of ∼100 m scale rather than ∼100 km) yields higher accretion rates due to enhanced capture rate by gas (Fortier et al. 2013; Chen et al. 2025), but using such small planetesimals to drive planet formation is in conflict with the observed characteristic 100 km scale of asteroids (Bottke et al. 2005; Johansen et al. 2015).

The pebble accretion theory was developed as a solution to the inefficiency of planetesimal accretion (using nominal sizes of 100 km) in forming the cores of giant planets within the lifetime of the protoplanetary disc, while avoiding the cores from migrating to the terrestrial planet zone (Johansen & Lacerda 2010; Ormel & Klahr 2010; Lambrechts & Johansen 2012). In pebble accretion, gas drag greatly enhances the accretion cross-section of millimetre- to centimetre-sized pebbles relative to larger planetesimals. High pebble accretion rates onto planetesimals and small protoplanets nevertheless require low turbulence strengths in the outer regions of the protoplanetary disc where the cores of gas giants grow (Lambrechts & Johansen 2014; Ormel 2017; Chambers 2018; Johansen & Lambrechts 2017; Gurrutxaga et al. 2024; Zhao & Matsumura 2025), since these small bodies initially accrete in the 3D regime where the local pebble density is set by the balance between sedimentation and turbulent diffusion. Such weak disc turbulence has indeed been inferred from observations of a high degree of pebble sedimentation in some protoplanetary discs (Pinte et al. 2016; Villenave et al. 2022). However, inferring the level of turbulence in protoplanetary discs is not straightforward and relies on many assumptions, for example about the pebble sizes and gas surface densities. In addition, the turbulence level in protoplanetary discs likely varies from disc to disc, between the inner and outer regions and over the evolutionary stage (Villenave et al. 2023; Bosman et al. 2023; Villenave et al. 2025; Jiang et al. 2025). Pebble accretion can also contribute significantly to the growth of rocky planets, super-Earths and sub-Neptunes in the inner disc (Lambrechts et al. 2019; Johansen et al. 2021; Izidoro et al. 2021; Nielsen et al. 2025; Danti et al. 2025), but the growth rate by pebble accretion relative to the rate of planetesimal accretion and giant impacts in the inner disc depends on pebble sizes and turbulence levels (Yap & Batygin 2024), and on the assumed population of planetesimals that forms in the inner disc.

In summary, the operation of both the streaming instability and pebble accretion have, since their discovery, been probed in great detail using computer simulations. Particularly, the conditions for filament formation by the streaming instability and efficient pebble accretion in terms of Stokes number, turbulence strength, and metallicity are now relatively well understood. These conditions are nevertheless rarely explored in the combined light of driving both streaming instability and pebble accretion. The goal of this paper is therefore to provide a better map of the outcome of planet formation as a function of the range of plausible conditions in the protoplanetary disc. We believe that this endeavour gives important insights into the influence of the protoplanetary disc environment on the formation of planetary systems.

The paper is organized as follows. In Sect. 2 we describe the protoplanetary disc model that we used to calculate the conditions for the streaming instability and the growth of planetary systems by pebble accretion. In Sect. 3, we go on to explore the conditions for the forming planetesimals by the streaming instability at the water ice line. In Sect. 4 we calculate the growth timescale of planetesimals formed by the streaming instability, highlighting a new result that the characteristic mass of planetesimals formed by the streaming instability is of similar magnitude to the threshold mass for efficient pebble accretion. In Sect. 5, we present synthetic populations of planetary systems formed by pebble accretion for a range of protoplanetary disc parameters. In Sect. 6, we map the conditions for the streaming instability and the outcome of pebble accretion simulations for a large range of pebble Stokes numbers and turbulence levels. Finally, in Sect. 7 we briefly summarize the key findings of the paper.

2. The protoplanetary disc model

We calculate the conditions in an evolving protoplanetary disc at the orbital distance of a planetesimal or a protoplanet using the analytical expressions derived in Gurrutxaga et al. (2024). That model uses a viscous α-disc approach to the gas combined with an exact analytical expression for the evolution of the pebble surface density in response to gas drag and radial drift. We assume here that the product of Stokes number St and logarithmic pressure gradient $\chi = -\partial \ln P/\partial \ln r$ is constant. This yields a relatively constant Stokes number in the inner disc followed by a radially declining Stokes number in the exponentially tapered outer regions of the disc where the pressure gradient increases; such a decline was demonstrated in Gurrutxaga et al. (2024) to give a good match to a more advanced coagulation model presented in Appelgren et al. (2023) that took into account that pebbles in the outer disc are limited in growth by the drift barrier rather than by the fragmentation barrier. We note that we must ignore the explicit temperature dependence of fragmentation-limited pebble growth in Eq. (1) in order exploit the analytical pebble flux expressions from Gurrutxaga et al. (2024).

2.1. Evolution of gas and pebbles

The ratio of pebble surface density to gas surface density Z is, surprisingly, independent of distance to the star when the product $\mathrm{St}\chi \equiv \mathrm{St}_\chi$ is assumed constant, and takes the temporal form

$$Z(t) = Z_0 T_{\rm e}^{-\frac{b_0}{2(2-\gamma)}}, \tag{2}$$

where Z_0 is the initial surface density ratio, $\gamma = 15/14$ is the power-law exponent of the viscosity and $b_0 = (2/3)\mathrm{St}_\chi/\alpha$ is a constant that compares the radial drift speed of the pebbles (through St_χ) to the radial accretion speed of the gas (through α). The dimensionless evolutionary time $T_{\rm e}$ is defined as

$$T_{\rm e} = t/t_{\rm s} + 1, \tag{3}$$

with t representing physical time and $t_{\rm s}$ denoting the viscous timescale over the initial disc size R_1,

$$t_{\rm s} = \frac{1}{3(2-\gamma)^2}\frac{R_1^2}{\nu_1} = 0.75\,{\rm Myr}\left(\frac{R_1}{100\,{\rm AU}}\right)^{13/14}\left(\frac{\alpha}{0.01}\right)^{-1}\left(\frac{L}{L_\odot}\right)^{-2/7}. \tag{4}$$

Here, $\nu_1 = \alpha c_{\rm s,1} H_1$ is the viscosity evaluated at the initial radius R_1. The luminosity scaling comes from adopting the irradiated temperature profile from Ida et al. (2016). The characteristic size of the disc $R_{\rm c}$ increases with time as

$$R_{\rm c}(T_{\rm e}) = R_1 T_{\rm e}^{1/(2-\gamma)}. \tag{5}$$

We have chosen to adopt an α-disc model for the gas due to its relative simplicity with only two free parameters governing its evolution: the dimensionless viscosity α and the initial disc size R_1. The α-disc model captures well the accretion of gas onto the star, with a speed proportional to the choice of α (Hartmann et al. 1998; Johansen et al. 2019). Angular momentum transport is nevertheless in reality most likely not facilitated by turbulent viscosity, as envisioned in the α-disc approach, but rather by magnetocentrifugal disc winds (Béthune et al. 2017; Mori et al. 2019). An analytical protoplanetary disc evolution model including loss of angular momentum and mass by disc winds was derived in Tabone et al. (2022) and used to calculate pebble accretion growth tracks in Zhao & Matsumura (2025). Other versions of disc wind models have also been derived (Chambers 2019). Although a disc wind model is more realistic than the α-disc model, it comes at the expense of introducing two additional free parameters ($\alpha_{\rm DW}$ that quantifies the gas accretion speed due to disc winds and λ that measures the angular removal efficiency of the wind and hence dictates also the amount of gas lost to the wind). We therefore use the simpler α-disc model in this paper, but we distinguish between an accretion α that dictates the speed of the gas, and hence the gas surface density for a given mass accretion rate onto the star, and a turbulent δ that measures the turbulent diffusion coefficient, and hence the scale height of the pebbles. In this picture, the gas disc may still evolve rapidly under a high value of the viscous α, even if the turbulence level δ is low.

2.2. Disc temperature

The temperature of the protoplanetary disc is given by a combination of stellar irradiation and viscous heating. For the former, we follow the temperature expression of Ida et al. (2016), with the luminosity of the star following Johansen et al. (2021),

$$L(t) = 2\,L_\odot\left(\frac{t}{\rm Myr}\right)^{-0.7}\exp\left[-\frac{1}{t/(0.15\,{\rm Myr})}\right]. \tag{6}$$

The first power-law term, which is an approximate fit to the stellar evolution database of Baraffe et al. (2015) for a solar-mass star, dominates after 0.5 Myr, while we added the exponential decline term to avoid excessive luminosities at earlier times. We compared our results to the luminosity model of Mori et al. (2021), which has a higher initial luminosity of the protostar, and found no significant difference to the resulting planet populations.

The viscous heating temperature, relevant in the inner regions of the disc for the earliest evolution stages, is calculated from Eq. (B.10) in Liu et al. (2019a), with the effective accretion rate that leads to heating calculated as the full accretion rate multiplied by δ/α to distinguish between wind-driven angular momentum transport with parameter α and turbulent heating with parameter δ. Above $T = 800\,{\rm K}$ we set $\delta = \alpha$ to reflect the onset of angular momentum transport by turbulence caused by the magnetorotational instability (Desch & Turner 2015). The region of active MRI turbulence is nevertheless small and short-lived and hence not very important for the outcome of our planet formation calculations.

Adopting an evolving temperature and including viscous heating in the inner disc is not formally consistent with the analytical evolution of the α-disc, but since the temperature evolution is generally small, we choose (as in Liu et al. 2019a) to use the temperature evaluated for a stellar luminosity $L_\star = L_\odot$ at the initial disc size R_1 to obtain an approximation for the viscous evolution of the protoplanetary disc over its full lifetime. We additionally adopt the temporally declining analytical pebble flux from Gurrutxaga et al. (2024) when constructing the pebble column density in the inner, viscously heated disc; the higher temperature in the inner disc will increase the pebble speed and thereby decrease the local value of Z slightly there compared to the outer disc.

2.3. Pebble flux

We show the pebble flux $\dot{\mathcal{M}}_{\rm p}$ through the inner regions of the protoplanetary disc as a function of time in Fig. 1 for three values of St = 0.003, 0.01, 0.03, and three values of the initial disc size R_1. The three initial disc sizes correspond to a starting stellar accretion rate of $\dot{\mathcal{M}}_{\star 0} = 10^{-7}\,M_\odot\,{\rm yr}^{-1}$ that falls to $\dot{\mathcal{M}}_{\star 5} = 5\times10^{-9}\,M_\odot\,{\rm yr}^{-1}$ (large disc), $\dot{\mathcal{M}}_{\star 5} = 2\times10^{-9}\,M_\odot\,{\rm yr}^{-1}$ (medium-sized disc) and $\dot{\mathcal{M}}_{\star 5} = 10^{-8}\,M_\odot\,{\rm yr}^{-1}$ (very large disc) after 5 Myr of evolution. For the smallest value of St, the pebble flux follows approximately the constant metallicity expression $\dot{\mathcal{M}}_{\rm p}(t) = Z_0\dot{\mathcal{M}}_\star(t)$. Pebbles with larger St drain from the protoplanetary disc faster than the accretion timescale of the gas, decreasing the pebble metallicity with time. The calculation presented in Fig. 1 used, for simplicity, a constant stellar luminosity of $L_\star = L_\odot$ and ignored viscous heating in the inner disc, while the models presented in Sects. 5 and 6 include viscous heating and use the evolving luminosity from Eq. (6).

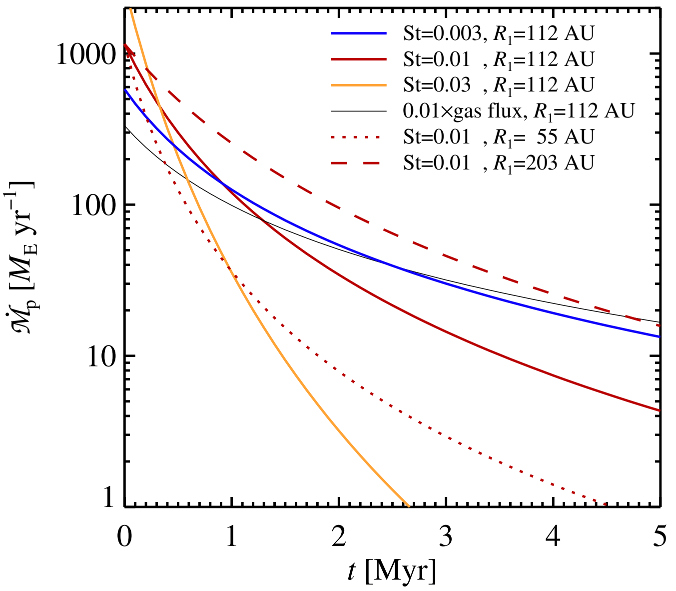

Fig. 1. Pebble flux $\dot{\mathcal{M}}_p$ through the inner disc as a function of time for three values of St (St = 0.003, St = 0.01, St = 0.03) and three different initial protoplanetary disc sizes (R_1 = 112 AU, R_1 = 55 AU, R_1 = 203 AU) for the analytical pebble drift model of Gurrutxaga et al. (2024) with constant St_χ and $\alpha = 0.01$. The thin black line indicates 1% of the gas flux for the 112 AU disc; the St = 0.003 case follows gas depletion closely due to the limited radial drift. Larger pebbles drain out of the disc by radial drift on a shorter timescale than the gas evolution time.

3. Conditions for the streaming instability

A prominent behaviour of the streaming instability is that dense, planetesimal-forming filaments only emerge in the sedimented mid-plane layer of pebbles when the average pebble metallicity, defined as the ratio of the surface density of pebbles to the surface density of gas, is above a threshold value (Johansen et al. 2009b; Bai & Stone 2010), which is of order ~1% but depends on the Stokes number (Carrera et al. 2015; Li & Youdin 2021) as well as on the presence/strength of any background turbulence (Johansen et al. 2007; Yang et al. 2018; Schäfer & Johansen 2022; Lim et al. 2024; Eriksson et al. 2026). We analyse here how the pebble metallicity in the inner regions of a protoplanetary disc depends on the properties of the disc and the pebble sizes. In Sect. 6, we show a map of how planetesimal formation by the streaming instability and planetary growth by pebble accretion depend on both the pebble Stokes number and on the strength of the turbulence in the disc. We use there the pebble metallicity threshold of Li & Youdin (2021), which also agrees with simulations of weak turbulence (δ between 10^{-4} and 10^{-3}) driven by the magnetorotational instability (Johansen et al. 2007; Eriksson et al. 2026).

3.1. Planetesimal formation at the water ice line

The water ice line provides an excellent location to achieve a local metallicity increase, as there the pebbles slow down and pile up if their Stokes number changes upon losing the ice component (Ida & Guillot 2016). The released water vapour will also pile up inside of the ice line, with the possibility that the vapour diffuses outwards across the water ice line and increases both the sizes and the metallicity of the icy pebbles there (Ros & Johansen 2013; Schoonenberg & Ormel 2017; Drążkowska & Alibert 2017). In order to assess the potential metallicity increase at the water ice line without resorting to 3D hydrodynamical simulations or evolving 1D disc simulations with turbulent diffusion, we calculate the density of silicate pebbles and water vapour inside of the water ice line under the assumption that the flux of these components inside of the water ice line is equal to the pebble flux across the ice line. We add silicate pebbles and water vapour together as an estimate of the upper limit to the pebble enrichment that can be reached, since this combined metallicity is the highest achievable by diffusion of water vapour across the ice line. In addition, water vapour inside of the water ice line will condense onto the silicate particles after the star undergoes a sudden decrease in its luminosity. Ros & Johansen (2024) studied the effect of cooling after a stellar outburst and found that icy particles could grow up to St = 0.03 by ice condensation and sweep-up of silicate dust aggregates. Given the lack of experimental support for considering a lower fragmentation threshold for silicates than for water ice (see discussion in Sect. 1), we consider silicate particles and combined silicate-ice particles to have the same Stokes number.

3.2. Temporal evolution of the metallicity

In Fig. 2, we show the temporal evolution of the metallicity outside (at 5 AU) and inside (at 0.5 AU) the water ice line for three values of the global Stokes number (St = 0.003, St = 0.01 and St = 0.03) and two combinations of disc viscosity and turbulence ($\alpha = 10^{-2}$ / $\delta = 10^{-4}$ and $\alpha = 10^{-3}$ / $\delta = 10^{-3}$). We set the initial and final accretion rate to $\dot{\mathcal{M}}_{\star 0} = 10^{-7}\,M_\odot\,\mathrm{yr}^{-1}$ / $\dot{\mathcal{M}}_{\star 5} = 5 \times 10^{-9}\,M_\odot\,\mathrm{yr}^{-1}$ when $\alpha = 10^{-2}$ and $\dot{\mathcal{M}}_{\star 0} = 10^{-8}\,M_\odot\,\mathrm{yr}^{-1}$ / $\dot{\mathcal{M}}_{\star 5} = 4.85 \times 10^{-9}\,M_\odot\,\mathrm{yr}^{-1}$ when $\alpha = 10^{-3}$ in order to maintain the same disc size (112 AU) and initial disc mass (~500 M_E of solids) for the two values of α. The metallicity inside of the water ice line includes, as discussed above, the sublimated water vapour. The three blue lines show the evolution of the metallicity as a function of time at a representative distance of 5 AU, based on the analytical solution for the pebble flux from Gurrutxaga et al. (2024). The global metallicity outside of the water ice line starts at the initial metallicity $Z_0 = 0.01$, but falls rapidly with time for St = 0.01 and St = 0.03, particularly for the model with $\alpha = 10^{-3}$ due to the much slower outward gas speed in the outer disc. This viscous expansion of gas and dust helps to store a large pebble reservoir in the outer disc, so that the pebble flux through the inner disc is lower and longer-lasting (Liu et al. 2022). In contrast, small pebbles with St = 0.003 drift so slowly relative to the gas, for both the high- and low-α case, that the pebble metallicity is maintained much better over the 5 Myr lifetime of the protoplanetary disc.

The conditions inside of the water ice line are more conducive to planetesimal formation than the outer regions, particularly if the Stokes number of the pebbles outside of the ice line is large, so that the pebble flux over the ice line is high. If the water vapour were to freeze out on the pebbles, as may happen in the cooling phase after a stellar luminosity outburst (Ros & Johansen 2024), while maintaining the metallicity of $Z = 0.02$–0.03, then planetesimal formation could be triggered at the water ice line for turbulence values δ between 10^{-5} and 10^{-4} (see Sect. 6). The situation becomes better at lower α (lower panel of Fig. 2): pile-ups are stronger due to slower gas speed. We nevertheless show in Sect. 5 that models with low α in the inner disc and a high $\dot{\mathcal{M}}_\star$ have very high planetary migration rates and hence struggle to maintain planets in the 1 AU region.

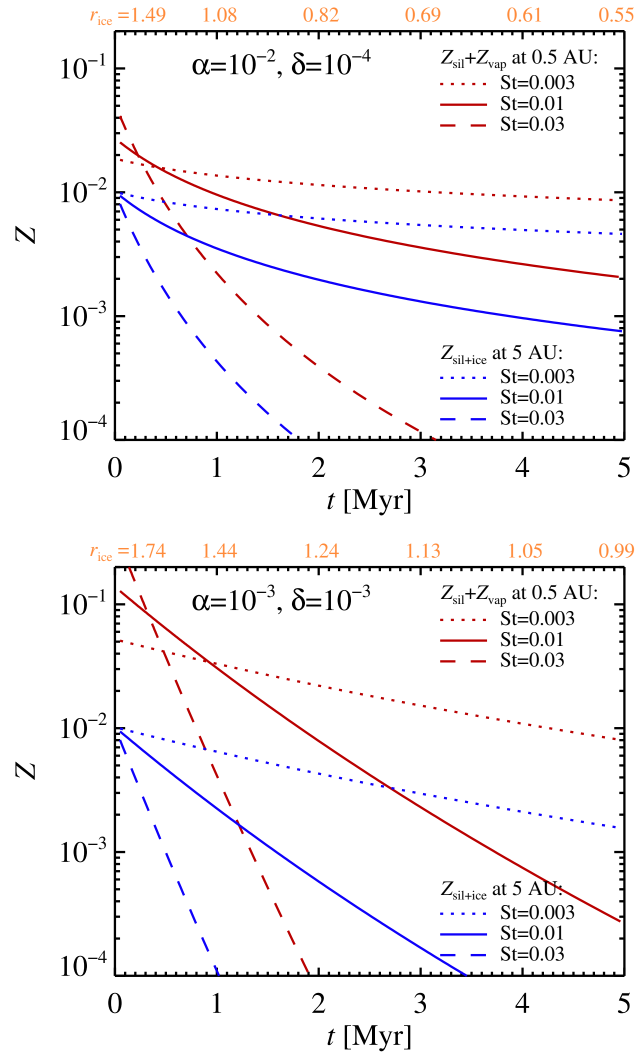

Fig. 2. Temporal evolution of the pebble metallicity in a large protoplanetary disc (R_1 = 112 AU) at 5 AU (outside of the water ice line, blue lines) and at 0.5 AU (inside of the water ice line, red lines) for two different combinations of the viscosity coefficient (α) and the turbulent diffusion coefficient (δ). Water vapour released at the passage of the water ice line is included in the metallicity at 0.5 AU. The instantaneous position of the water ice line is indicated above the plots. The high viscous heating in the case $\alpha = \delta = 10^{-3}$ (*bottom*) pushes the ice line out, while the lower speed of the gas allows for a much bigger pile-up of water vapour inside of the water ice line.

3.3. Formation of planetesimals beyond the water ice line

Clearly, planetesimal formation cannot operate only around the water ice line and is also required to function further out in the disc. Planetesimal formation in the 10–100 AU region may become easier at the higher-than-solar metallicity reached by stars formed relatively recently in our Galaxy. The presence of pressure bumps in the outer disc regions, emerging perhaps from inverse cascade of magnetic energy in weak magnetorotational turbulence (Lyra et al. 2008a; Johansen et al. 2009a; Eriksson et al. 2026), could facilitate the formation of planetesimals there. The CO and CO_2 ice lines are also prime candidates for metallicity increases similar to what occurs at the water ice line (Stammler et al. 2017; Schneider & Bitsch 2021). We nevertheless do not study the conditions for planetesimal formation around these colder ice lines in this paper, since that would require a more realistic model of pebble and vapour pile-ups in the outer disc.

4. Planetesimal masses and growth timescales

We now turn to analysing the characteristic mass of planetesimals that form by the streaming instability as well as their initial growth timescale.

4.1. Planetesimal masses

Most hydrodynamical simulations of the streaming instability are performed in the local shearing box frame where the natural length-scale is the gas scale-height H and the natural density scale is the local mid-plane gas density ρ_g (Johansen et al. 2015; Simon et al. 2016; Li & Youdin 2021); the right-hand-side of the Poisson equation for the self-gravity of the pebbles ($\nabla^2 \Phi = 4\pi G \rho_p$) can then be rewritten as the dust-to-gas ratio $\epsilon = \rho_p/\rho_g$ times the dimensionless self-gravity parameter,

$$\Gamma = \frac{4\pi G \rho_g}{\Omega^2} = \frac{4G\dot{\mathcal{M}}_\star}{3\sqrt{2\pi}\alpha c_s H^2 \Omega^2} = \frac{4G\dot{\mathcal{M}}_\star}{3\sqrt{2\pi}\alpha c_s^3} \approx 0.11 \left(\frac{\dot{\mathcal{M}}_\star}{10^{-7}\,M_\odot\,\mathrm{yr}^{-1}}\right)\left(\frac{\alpha}{10^{-2}}\right)^{-1}\left(\frac{T}{100\,\mathrm{K}}\right)^{-3/2} . \tag{7}$$

The second equality relation is valid for the inner regions of an α-disc where the gas density is related to the gas accretion rate through $\dot{\mathcal{M}}_\star = 3\pi\nu\Sigma_g = 3\pi(\alpha c_s H)(\sqrt{2\pi}H\rho_g)$. Liu et al. (2020) analysed a range of literature results on the masses of planetesimals formed by the streaming instability, published by different groups (using also independent codes), and found that the characteristic mass of planetesimals follows the approximate expression

$$M_{SI} = 5\times10^{-5} M_E \left(\frac{\Gamma}{\pi^{-1}}\right)^{1.5}\left(\frac{H/r}{0.05}\right)^3\left(\frac{M_\star}{M_\odot}\right). \tag{8}$$

We fix the stellar mass to $M_\star = M_\odot$ from now on.

Using $c_s \propto r^{-3/14}$ and $H/r \propto r^{2/7}$ from the temperature profile of Ida et al. (2016), Eq. (8) reveals a radius scaling $M_{SI} \propto r^{51/28}$ with the exponent $51/28 \approx 1.82$. The full scaling of the planetesimal mass of Eq. (8), with the temperature profile embedded, becomes

$$M_{SI} = 4.5\times10^{-7} M_E \left(\frac{\dot{\mathcal{M}}_\star}{10^{-7}\,M_\odot\,\mathrm{yr}^{-1}}\right)^{1.5}\left(\frac{\alpha}{10^{-2}}\right)^{-1.5} \times\left(\frac{L_\star}{L_\odot}\right)^{-3/14}\left(\frac{r}{\mathrm{AU}}\right)^{51/28} . \tag{9}$$

We show in Fig. 3 the characteristic planetesimal mass formed by the streaming instability from 1 AU to 100 AU around a solar-mass star at an early disc evolution stage where $\dot{\mathcal{M}}_\star = 10^{-7}\,M_\odot\,\mathrm{yr}^{-1}$.

4.2. Growth timescale

We show in Fig. 3 also the e-folding growth timescale by pebble accretion of a planetesimal or protoplanet of mass M (based on Johansen & Lambrechts 2017), defined as $\tau_{grow} = M/\dot{M}$, for two different values of the Stokes number St. For simplicity, we use a constant pebble Stokes number (St = 0.01 or St = 0.1), constant turbulence strength ($\delta = 10^{-4}$) and constant pebble metallicity

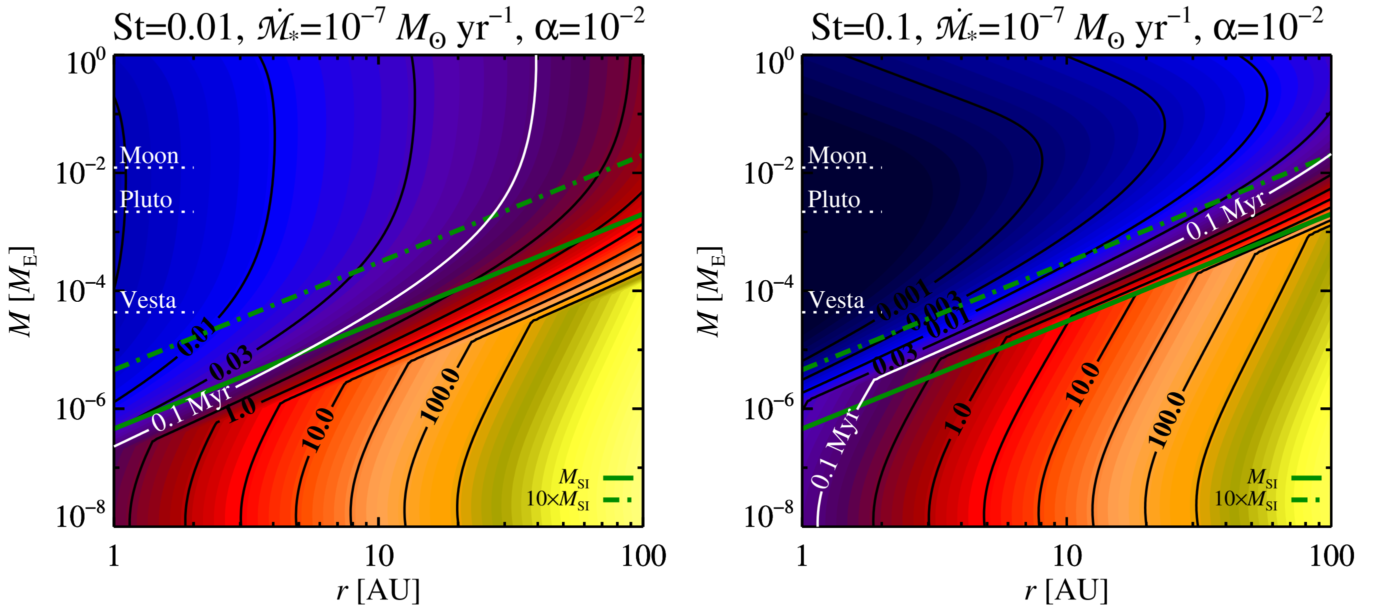

Fig. 3. Growth timescale of planetesimals as a function of their distance to the star and their mass (colours and contours), overplotted with the characteristic mass of planetesimals formed by the streaming instability (green line) and ten times the characteristic mass to represent the upper end of the initial mass function (green dash-dotted line). *Left*: Growth timescales for St = 0.01 *Right*: Growth timescales for St = 0.1. We highlight the 0.1 Myr contour line as a threshold timescale that demarcates efficient planetary growth from inefficient growth at lower masses due to the transition the loosely coupled Bondi regime of pebble accretion.

($Z = 0.01$) across the protoplanetary disc and set the stellar luminosity equal to the current solar luminosity (ignoring the early stellar luminosity evolution from Eq. (6)).

Overall, Fig. 3 demonstrates that growth timescales increase from ~0.03 Myr to ~3 Myr between 1 AU and 100 AU for St = 0.01 at the characteristic mass of the streaming instability, and that the growth timescales are significantly longer at the streaming instability mass for the higher St = 0.1. However, for both values of St, the growth timescales drop dramatically at just ten times the characteristic mass. Considering instead lower initial masses, Fig. 3 also implies that a putative generation of low-mass planetesimals, similar to the objects in the classical Kuiper Belt, formed at the late evolutionary stages of the protoplanetary disc with a low value of Γ (Carrera et al. 2017; Johansen et al. 2025; Li & Chiang 2025) would undergo very little growth by pebble accretion.

The most massive planetesimals formed by the streaming instability are indeed typically at least 10 times more massive than the characteristic mass (Schäfer et al. 2017; Liu et al. 2020; Schäfer et al. 2024). We therefore use 20 times the streaming instability mass as the nominal starting point for our pebble accretion calculations in Sects. 5 and 6, and we emphasize that the planetesimal starting mass is very important, since the rather massive planetesimals formed by the streaming instability do not grow appreciably by mutual collisions beyond a few AU in the protoplanetary disc (Lorek & Johansen 2022; Kaufmann et al. 2025).

4.3. Pebble accretion threshold mass

As demonstrated in Lyra et al. (2023), the inclusion of a size distribution of pebbles can actually decrease the growth timescale, particularly for large values of St. The reason is that there exists a planetesimal mass scale below which the pebbles couple to the gas flow on longer timescales than the scattering process, which diminishes the kinetic energy dissipation and hence reduces the pebble accretion cross-section significantly. This pebble accretion threshold mass $M_{\rm PA}$ is given by the condition

$$\frac{GM_{\rm PA}}{(\Delta v)^3} = \tau_{\rm f}, \tag{10}$$

where we equalled the timescale to cross the Bondi radius, $t_{\rm B} = R_{\rm B}/\Delta v = GM/(\Delta v)^3$, to the friction time $\tau_{\rm f}$. The approach speed Δv equals the sub-Keplerian speed of the pebbles if the planetesimal itself is low mass and on a circular and non-inclined orbit. This yields a mass for the onset of pebble accretion of

$$M_{\rm PA} = \frac{{\rm St}\,(\Delta v)^3}{G\Omega} \approx 1.6\times10^{-6}\,M_{\rm E}\left(\frac{\rm St}{0.01}\right)\left(\frac{r}{\rm AU}\right)^{12/7}. \tag{11}$$

We did not include here a numerical factor of 1/8 that is sometimes included in the expression for the loose coupling mass (Ormel 2017; Lyra et al. 2023). Both the mass prefactor ($1.6\times10^{-6}\,M_{\rm E}$) and the distance exponent $12/7 \approx 1.71$ are surprisingly close to the characteristic mass of planetesimals formed by the streaming instability from Eq. (9).

4.4. Similarity between the streaming instability mass and the pebble accretion threshold mass

The similarity between the loose coupling mass of pebble accretion and the characteristic mass of the streaming instability is actually not a coincidence. We expect that the mass of planetesimals formed by the streaming instability should broadly take the form

$$M_{\rm SI} \sim \rho_{\rm R}(\eta r)^3(\rho_{\rm g}/\rho_{\rm R})^p. \tag{12}$$

Here, $\rho_{\rm R} = 9\Omega^2/(4\pi G)$ is the Roche density, which must be reached before a portion of a dense pebble filament can undergo full 3D collapse into a planetesimal. The characteristic scale of a filament formed by the streaming instability is $\ell_{\rm SI} = \eta r$ (Youdin & Goodman 2005), where $\eta = -(1/2)(H/r)^2 \partial \ln P/\partial \ln r$ is a measure of the radial pressure support of the gas, which feeds streaming motion between gas and pebbles. The sub-Keplerian speed of the gas, in the absence of drag-force from the pebbles, is given by $\Delta v = \eta v_{\rm K}$. However, the pebble density in the mid-plane of the protoplanetary disc is similar to the mid-plane gas density $\rho_{\rm g}$, which is orders of magnitude below the Roche density. We therefore posit that the filament has to undergo first a radial contraction before reaching the Roche density, shrinking initially only its radial extent by a factor $\rho_g/\rho_{\rm R} = (1/9)\Gamma$. Following this radial contraction to reach the Roche density, further isotropic collapse from a sphere of density $\rho_{\rm R}$ and length-scale $\ell_{\rm R} = \eta r(\rho_g/\rho_{\rm R})$ corresponds to $p = 3$ in Eq. (12), while smaller values of p imply that the planetesimal collects mass from the larger scale ηr in one or more directions. Computer simulations of the streaming instability are consistent with $p = 1.5$, as noted in the discussion of Eq. (8) above. This choice of $p = 1.5$ corresponds also to the value suggested in Klahr & Schreiber (2021), their Eq. (2), based on a model of how self-gravity has to operate on sufficiently large scales to overcome the turbulent diffusion generated by the streaming instability itself.

Using $\eta = \Delta v/v_{\rm K}$, Eq. (12) can now be converted to

$$M_{\rm SI} \sim \frac{9\Omega^2}{4\pi G}\frac{\Delta v^3}{\Omega^3}(\Gamma/9)^p \sim \frac{9^{1-p}}{4\pi}\frac{\Delta v^3}{G\Omega}\Gamma^p. \quad (13)$$

This expression has the same dependence on Δv and Ω as the pebble accretion threshold mass from Eq. (11), with the ratio

$$\frac{M_{\rm SI}}{M_{\rm PA}} = \frac{\Gamma^p}{\rm St}\frac{9^{1-p}}{4\pi} \approx 0.084\left(\frac{\rm St}{0.01}\right)^{-1}\left(\frac{\Gamma}{0.1}\right)^{1.5}. \quad (14)$$

Here we took $p = 1.5$ in the second equality. Hence, for a nominal Stokes number (St ~ 0.01) and a protoplanetary disc mass corresponding to the earliest stages of disc evolution ($\Gamma \sim 0.1$), the pebble accretion threshold mass is approximately 12 times the characteristic mass of planetesimals formed by the streaming instability; this order of magnitude difference is also clear from Fig. 3.

4.5. Constant pressure support

The scaling of the characteristic planetesimal mass from simulations, Eq. (8), with $(H/r)^3$ rather than $(\Delta v)^3$, as in Eq. (13), likely arises from the fact that the pressure support parameter $\Pi = \Delta v/c_{\rm s}$ is typically kept constant in shearing sheet simulations. This converts Eq. (13) to the form

$$M_{\rm SI} \sim \rho_{\rm R}\left(\frac{\Delta v}{c_{\rm s}}\right)^3 H^3(\Gamma/9)^p \sim M_\star \Pi^3\left(\frac{H}{r}\right)^3(\Gamma/9)^p. \quad (15)$$

The last equality came from expanding the Roche density to transform the H^3 scaling to an $(H/r)^3$ scaling similar to Eq. (8).

5. Outcome of pebble and gas accretion

We now investigate the growth of planetesimals by pebble accretion and gas accretion starting at the upper range of the initial mass of planetesimals formed by the streaming instability.

5.1. Model assumptions

Our algorithms used for calculating the pebble accretion and gas accretion rates, as well as the planetary migration rate and gap formation, follow Johansen & Lambrechts (2017), Ida et al. (2018) and Johansen et al. (2019). The pebble accretion algorithm includes both the 3D and 2D phases of the Bondi and Hill accretion regimes, with a smooth transition between them based on a calculation of the accretion impact parameter (Johansen & Lambrechts 2017). We ignore positive torques from the pebble flow close the planet, which can slow down or even reverse migration at Stokes numbers above St = 0.03 (Benítez-Llambay & Pessah 2018). We also ignore positive torques arising from viscous heating in the inner disc (Paardekooper et al. 2010, 2011; Bitsch et al. 2015), from the planetary accretion heat (Benítez-Llambay et al. 2015; Baumann & Bitsch 2020) as well as the torque reduction from the dynamical corotation torque (Paardekooper 2014). The latter has been demonstrated to potentially slow down Type I migration by a factor of ~2 (Ndugu et al. 2021; Yun et al. 2022), which motivates our exploration of models with a lower gas fraction (and hence slower migration) in Sect. 5.6. By not including multiple potential sources of positive torques from the gas, our study thus constitutes a worst case scenario considering planetary migration at the unabated Type I and Type II rates. We discuss this further in Sect. 7.

Gas accretion is allowed either when the mass of a protoplanet is higher than the local pebble isolation mass, whose dependence on temperature and viscosity is based here on Bitsch et al. (2018), or when the pebble accretion timescale is longer than 10 Myr (Gurrutxaga et al. 2024), which is often the case late in the evolution of the disc as the pebble flux diminishes. We set the opacity level in the envelope to $\kappa_{\rm env} = 0.005\,{\rm m^2\,kg^{-1}}$. A higher or lower opacity will slow down or speed up the Kelvin-Helmholtz gas contraction phase of the envelope (Ida et al. 2018; Johansen et al. 2019), but we checked that even factor of ten changes to the opacity will only change the final orbits of cold gas giants in our simulations by ~1 AU.

We use a nominal pebble metallicity of $Z = 0.01$, consisting of 50% silicate rock and metal and 50% water ice (Lodders 2003). The water ice fraction is removed from the pebbles when they reach the temperature of $T_{\rm ice} = 170\,{\rm K}$ in either the protoplanetary disc or at the radiative-convective boundary (RCB) in the gas envelopes of massive protoplanets. The temperature at the RCB is calculated as a function of the local disc properties, planet mass and accretion rate from the analytical expressions of Piso & Youdin (2014); our implementation is detailed in Johansen et al. (2023b).

We assume that all pebbles have the same product of Stokes number and logarithmic pressure gradient, with a nominal value of St = 0.01 at the characteristic disc radius $R_{\rm c}$. The slightly shallower pressure gradient in the main disc regions, inside of the characteristic radius $R_{\rm c}(t)$ (see Eq. (5)), yields then a Stokes number there that is approximately 30% higher than at $R_{\rm c}$. We ignore the presence of smaller dust grains in the size distribution and refer to Lyra et al. (2023) for a discussion of the role of the small end of the size distribution for pebble accretion. We do not consider the presence of any local pressure bumps in our growth track calculations (Jiang & Ormel 2023; Eriksson et al. 2026).

We also assume that the growing planets have near-zero eccentricity and near-zero inclination, as is indeed observed for the most massive bodies that grow by pebble accretion in N-body simulations (Levison et al. 2015; Liu et al. 2019b; Yzer et al. 2025; Lorek & Lambrechts 2026). The most important simplification of our work is therefore arguably that we ignore any interactions between the growing planets, which means that we cannot capture protoplanet collisions nor eccentricity and inclination excitation or trapping in resonant chains (Lambrechts et al. 2019; Bitsch et al. 2019; Izidoro et al. 2021). However, this simplification allows us to create population plots whose statistical properties can easily be compared to the Solar System and to exoplanets at the population level, although it gives no information about the range of architectures of actual planetary systems.

Our nominal protoplanetary disc model has viscous $\alpha = 10^{-2}$, an initial gas accretion rate of $\dot{\mathcal{M}}_{\star 0} = 10^{-7}\,M_\odot\,\mathrm{yr}^{-1}$ and a final accretion rate of $\dot{\mathcal{M}}_{\star 5} = 5 \times 10^{-9}\,M_\odot\,\mathrm{yr}^{-1}$ after 5 Myr of evolution. The initial size of such a disc is $R_1 = 112$ AU, representing a disc among the 10% largest observed at the class 0 and I phases (Najita & Bergin 2018; Bate 2018; Ohashi et al. 2023; Tobin & Sheehan 2024). Gas giant planets are quite rare at solar metallicity – only around 7% of solar-metallicity stars host a gas giant with a mass higher than Saturn's in the 1–5 AU region (Fulton et al. 2021) – hence we probe the largest (and thus rarest) protoplanetary discs for their formation. We also experiment with even larger discs (with final accretion rate $\dot{\mathcal{M}}_{\star 5} = 10^{-8}\,M_\odot\,\mathrm{yr}^{-1}$ and a size of 203 AU) as well as more nominal-sized discs (with final accretion rates $\dot{\mathcal{M}}_{\star 5} = 2 \times 10^{-9}\,M_\odot\,\mathrm{yr}^{-1}$ / $\dot{\mathcal{M}}_{\star 5} = 10^{-9}\,M_\odot\,\mathrm{yr}^{-1}$ and initial sizes 55 / 33 AU). The latter are more prone to forming super-Earths and sub-Neptunes as their upper mass range, rather than gas giants.

The turbulence level δ controls both the pebble scale-height and the turbulent heating of the protoplanetary disc. We explore turbulence strengths between $\delta = 10^{-5}$ and $\delta = 10^{-3}$. The lower and middle range of this interval is supported by observations of the scale-height of dust in two well-resolved edge-on protoplanetary discs (Pinte et al. 2016; Villenave et al. 2022), while the higher range represents conditions in a few well-resolved discs with high pebble scale-heights as well as the typical upper values from many discs with unresolved pebble scale-heights (Villenave et al. 2025).

5.2. Turbulence strength, planetesimal masses and disc size

Figure 4 shows the resulting planet populations for two different values of δ, namely $\delta = 10^{-5}$ (top panels) and $\delta = 10^{-4}$ (lower panels). For the lower value of δ, we observe the formation of rocky planets, super-Earths, sub-Neptunes, and hot and cold gas giants when using a starting planetesimal mass that is 20 times the characteristic mass from Eq. (8). The disc loses its cold gas giants in the 5 AU region when we start instead at 3 times the characteristic mass (top right panel of Fig. 4), highlighting the importance of the planetesimal starting mass and confirming that the planetesimal growth rates shown in Fig. 3 strongly affect the final planetary system. For the higher value of $\delta = 10^{-4}$ (bottom panels of Fig. 4), the disc also reduces the orbits of its gas giants, but the lower right plot shows that doubling the initial disc size to 203 AU reinstates Jupiter and Saturn analogues under such turbulent conditions.

The fact that cold gas giants require favourable conditions to form is further illustrated in Fig. 5. The top panel shows that increasing the strength of the turbulence to $\delta = 10^{-3}$, while maintaining a viscosity of $\alpha = 10^{-2}$, quenches the formation of all classes of gas giants: cold, warm and hot. The increased turbulence decreases the growth rates of protoplanets both by increasing the scale-height of the pebble mid-plane layer, which means that protoplanets spend more time in the 3D branch of pebble accretion, and by increasing the temperature in the inner disc by viscous heating, which decreases the Bondi radius for pebble accretion (Batygin & Morbidelli 2022; Danti et al. 2025). The increased temperature also increases the pebble isolation mass in the inner disc and makes it harder to form sub-Neptunes with small gas envelopes.

In the middle and bottom panels of Fig. 5, we instead decrease the initial disc size from $R_1 = 112$ AU to more median values of $R_1 = 55$ AU and $R_1 = 33$ AU. This removes first cold gas giants and, for the smallest initial size, even hot and warm gas giant become very rare. The colder conditions in the inner disc, compared to the case of increased turbulence strength, nevertheless still allow super-Earths and sub-Neptunes to form and migrate to hot orbits.

5.3. Water mass fraction

The water mass fraction is indicated with colours in the population plots. The water ice line (vertical dotted lines) starts at approximately 1.5 AU in the cold disc models of Fig. 4 and migrates to nearly 0.5 AU after 5 Myr of evolution, due mainly to the steadily decreasing stellar luminosity. All giant planets in Fig. 4 have very water-rich cores that have been assembled well beyond the water ice line. The super-Earths that migrate to the inner disc edge without accreting gas are all very dry, while the sub-Neptunes in hot orbits mainly have water-rich cores (Nielsen et al. 2025). In the 1 AU region, the water mass fraction decreases with increasing planet mass due to sublimation of ice from the accreted pebbles (Johansen et al. 2021; Wang et al. 2023; Johansen et al. 2023b). Earth likely contains a few thousand parts per million (ppm) of water, when including the dominant reservoir in the core, which corresponds roughly to the green colour in Fig. 4. At higher turbulence levels (lower right panel of Fig. 4), migration becomes more pronounced, due to lower pebble accretion rates, exposing the 1 AU region to water-rich (blue) interlopers that formed at so cold conditions that water vapour sublimated from the pebbles is released below the RCB, and hence cannot escape from the growing planet (Wang et al. 2023).

5.4. Reducing or increasing α

We continue to experiment with a lower value and a higher value of the angular momentum transport coefficient α. Figure 6 shows results with $\alpha = 10^{-3}$ and $\alpha = 10^{-1}$ inside of 5 AU, while we fix $\alpha = 10^{-2}$ in the outer disc in order to maintain the same pebble flux as in the top left panel of Fig. 4. We additionally choose to fix the initial planetesimal mass here at $M_0 = 10^{-3}\,M_\mathrm{E}$. This is done partially to prevent the value of α in the inner disc from affecting the planetesimal masses, through its effect on the self-gravity parameter Γ in Eq. (7), which would complicate the comparison between low and high α; and partially with the motivation to probe the effect of early collisional evolution within the protoplanetary disc (Lorek & Johansen 2022). For the lower value of α (top panel of Fig. 6), we also set the strength of the turbulence to $\delta = \alpha = 10^{-3}$ in order to mimic an inner disc where angular momentum is transported by turbulence rather than by disc winds. The combination of higher gas column densities and stronger turbulence leads to significant viscous heating of the inner disc. The ice line is pushed out to 1.5–3 AU. The top panel of Fig. 6 shows that pebble accretion is efficiently suppressed by the high temperatures in the inner regions of the disc (Batygin & Morbidelli 2022; Danti et al. 2025). Planets ending in orbits within 2 AU have all migrated

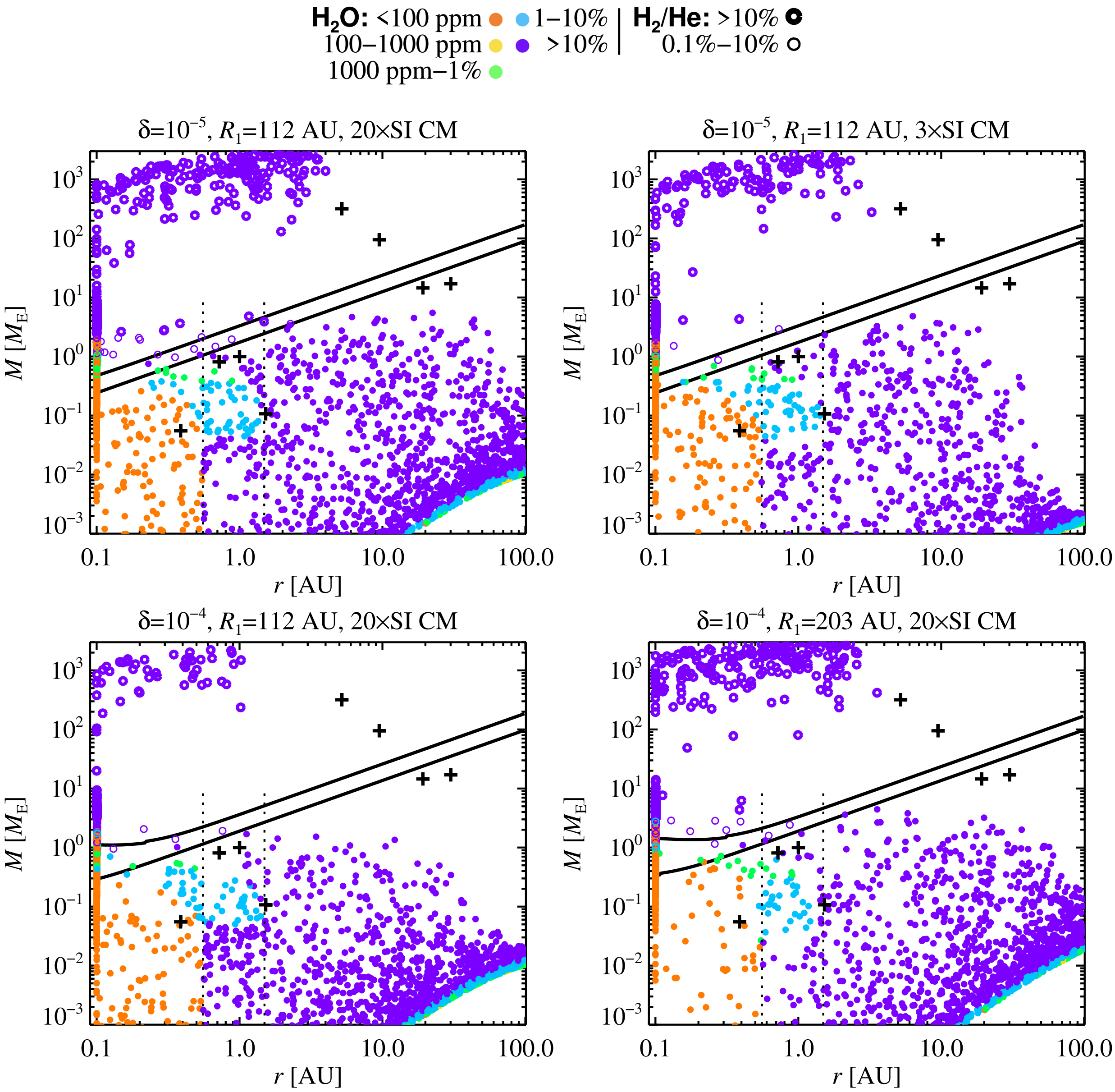

Fig. 4. *Top left*: population synthesis for a low turbulence level of $\delta = 10^{-5}$ and an initial planetesimal mass that is 20 times the characteristic mass of the streaming instability (SI CM). The colours indicate the water mass fraction in the non-gas material, while the open circles indicate two gas fraction intervals (see legend on top). The two black lines show the pebble isolation mass at early ($t = 0.3$ Myr) and late ($t = 5.0$ Myr) stages in the evolution of the disc, while the vertical dotted lines indicate the early and late locations of the water ice line. The Solar System planets are indicated with plus symbols. We see the emergence of all classes of planets, including cold gas giants similar to Jupiter and Saturn. *Top right*: result of decreasing the planetesimal masses to three times the characteristic mass. This has mainly the effect of reducing the planetesimal growth rates beyond 20 AU, due to the transition there towards the loose coupling branch of pebble accretion, which decreases the population of warm and cold gas giants. *Bottom left*: increasing the turbulence strength instead to $\delta = 10^{-4}$ suppresses the formation of cold gas giants. *Bottom right*: cold gas giants can form again with $\delta = 10^{-4}$ turbulence when the initial disc size is increased to $R_1 = 203$ AU.

there from more distant, and hence cooler and more water-rich, starting orbits. The bottom panel of Fig. 6 shows the effect of instead increasing the turbulent angular transport coefficient to $\alpha = 10^{-1}$. Such a fast gas accretion could correspond to angular momentum transport by strong discs winds facilitated by the Hall magnetohydrodynamics (MHD) effect in the inner regions of disc (Mori et al. 2019); we therefore set here a weaker turbulence level of $\delta = 10^{-4}$. Planetary migration is reduced due to the low gas column densities, and sub-Neptunes and super-Earths experience diminished migration, while smaller rocky planets do not migrate substantially from their starting point in such high-α conditions.

5.5. Lower metallicity

We now turn to exploring the effect of lowering the pebble metallicity to $Z = 0.005$. Figure 7 shows results for two values of the turbulence strength. At $\delta = 10^{-5}$, cold gas giants vanish, while warm and hot gas giants still form if they start their growth very early in the evolution of the disc. Increasing the turbulence level to $\delta = 3 \times 10^{-5}$ (lower panel of Fig. 7) removes also most of the warm gas giants. The populations of sub-Neptunes, super-Earths and rocky planets are nevertheless relatively unaffected by the lower metallicity (Liu et al. 2019a; Nielsen et al. 2023), which agrees well with observations of

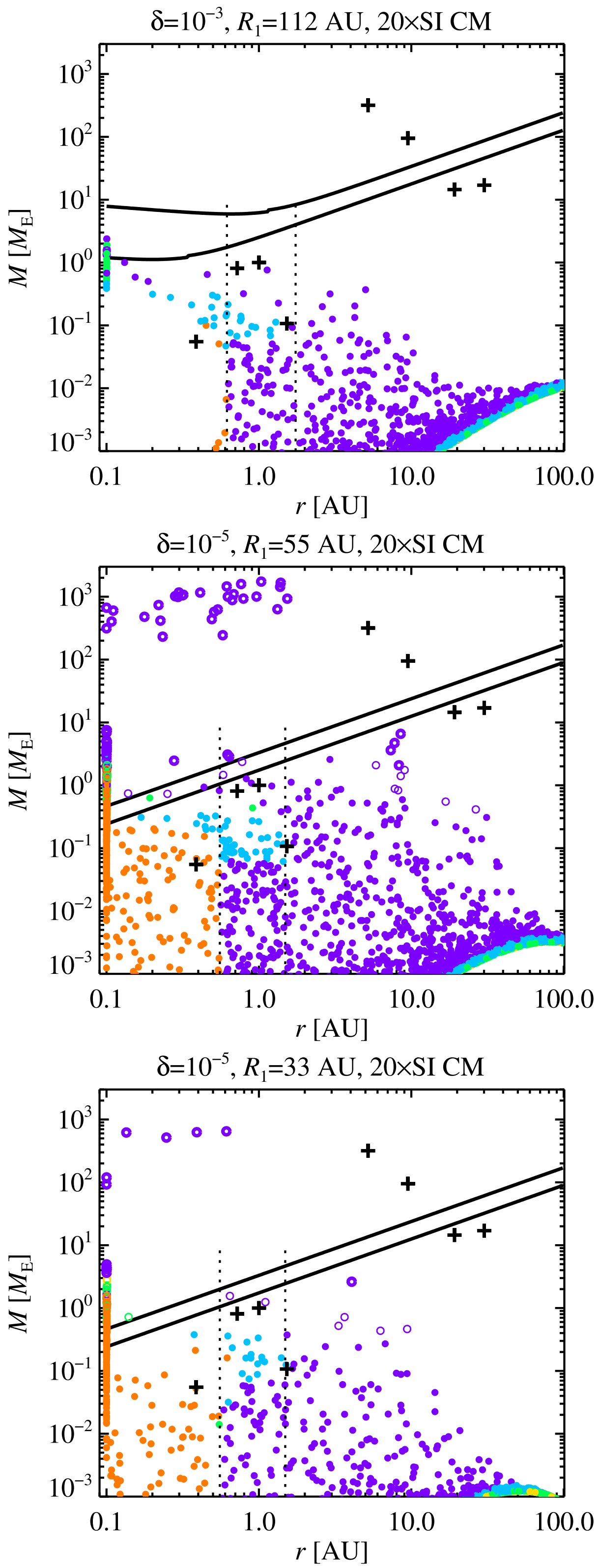

Fig. 5. Illustration of how increasing the turbulence level further than in Fig. 4 (to $\delta = 10^{-3}$; *top*) or lowering the initial disc size (to $R_1 = 55$ AU, *middle*, or $R_1 = 33$ AU, *bottom*) affects the ability of the disc to form planets via pebble accretion. Increasing the turbulence level also increases the temperature in the inner disc, which manifests in the top plot as a higher pebble isolation mass in the inner disc and a reduction of the pebble accretion rate there. The smaller discs with weaker turbulence, in contrast, retain their ability to form rocky planets, super-Earths, and sub-Neptunes.

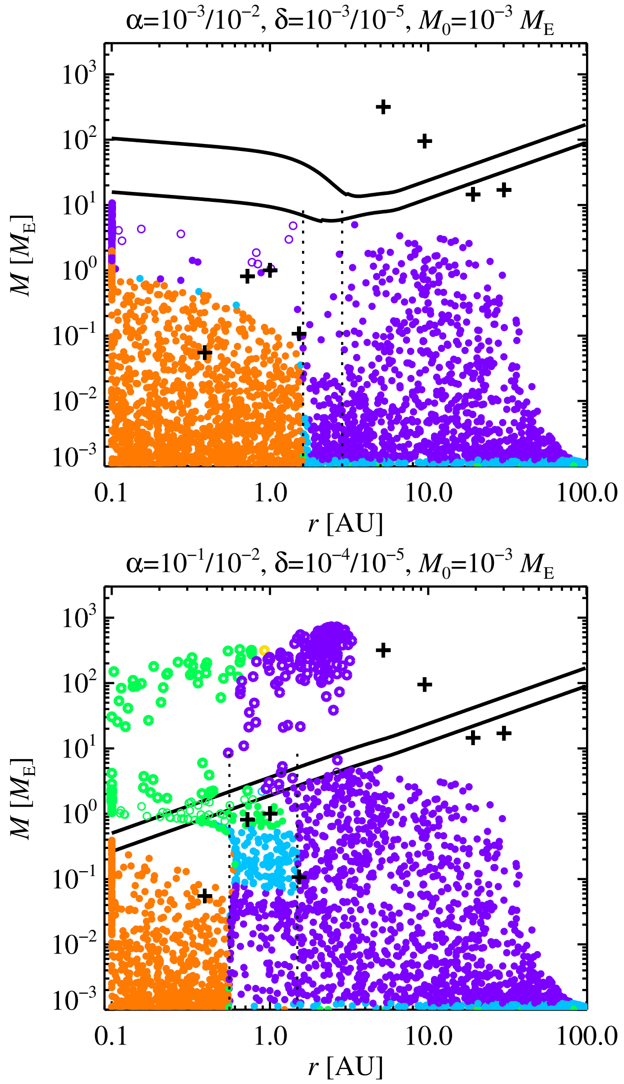

Fig. 6. Comparison of two models with angular momentum transport coefficient $\alpha = 10^{-2}$ outside of 5 AU and a lower value ($\alpha = 10^{-3}$; *top*) or a higher value ($\alpha = 10^{-1}$; *bottom*) inside of 5 AU. We fix the initial planetesimal mass to $M_0 = 10^{-3}\,M_E$ and the starting times between 0.5 and 5 Myr, to probe the effect of early collisional evolution. In the low-α case, we use $\delta = \alpha = 10^{-3}$ to additionally probe the effect of viscous heating, which pushes the ice line outwards to 1.5–3 AU. Pebble accretion is strongly suppressed by the high temperatures in the inner disc and all planets ending up in this region have migrated from more distant orbits beyond the water ice line. In the case of higher α, migration is strongly reduced due to lower gas column densities in the inner disc, which suppresses the migration of super-Earths and sub-Neptunes to the disc edge. Lower-mass rocky planets form more or less in situ with this reduced migration.

little or no metallicity-dependence for non-giant exoplanets (Buchhave et al. 2012).

5.6. Lower gas fraction

The planetary populations produced under various conditions in the protoplanetary disc in this section show as a common feature that forming cold gas giants by pebble accretion requires low turbulence and/or large initial disc sizes, while warm and temperate gas giants in ~0.1–1 AU orbits emerge readily even under conditions where cold gas giant formation is suppressed, highlighting migration as a key element in making formation

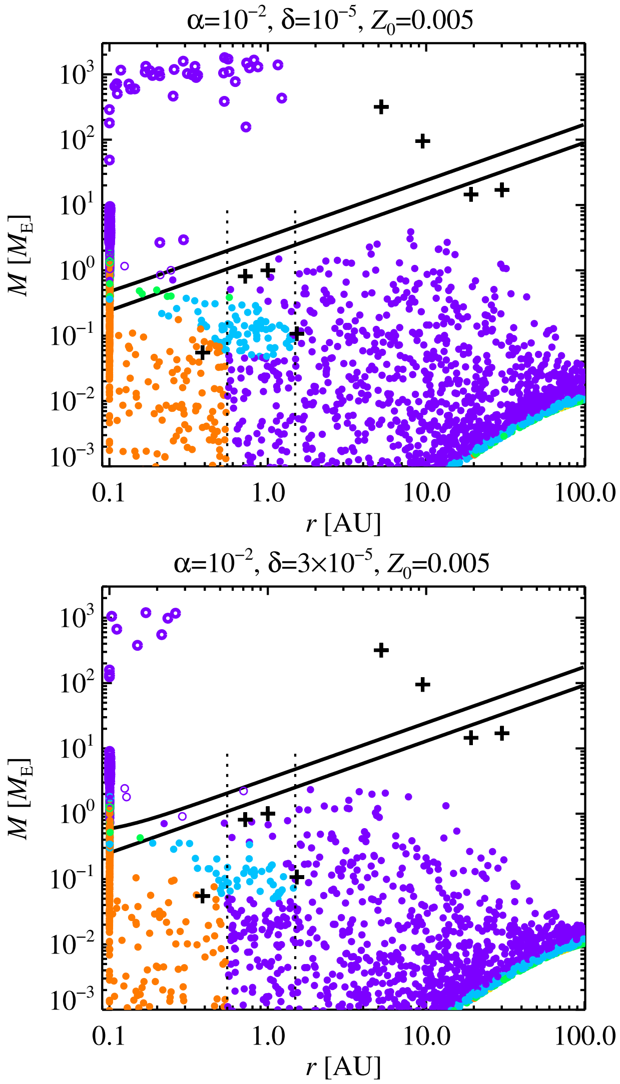

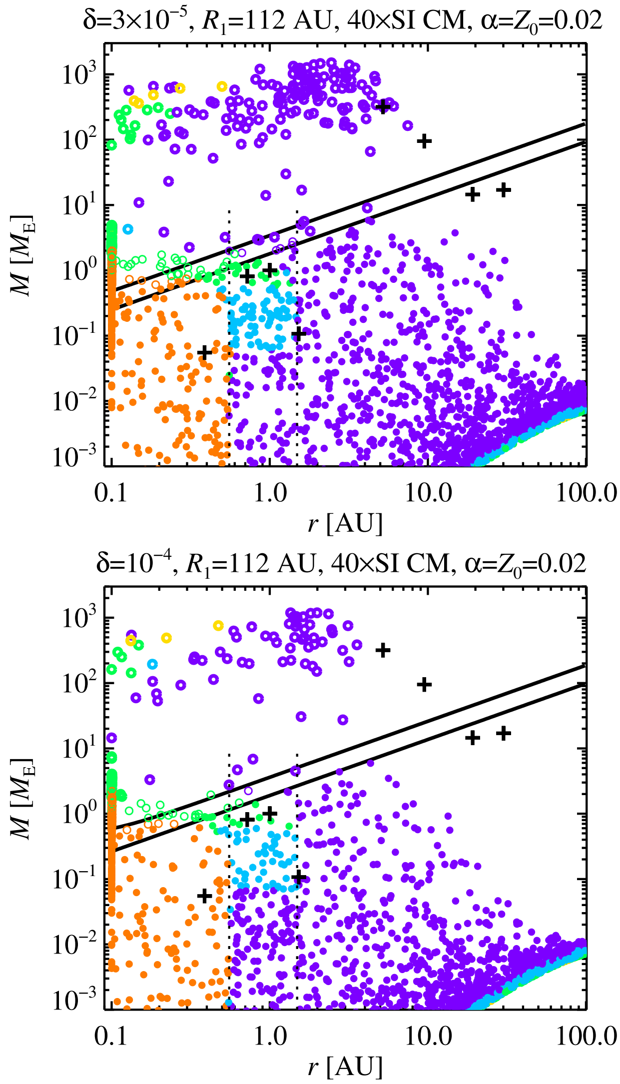

Fig. 7. Effect of halving the pebble metallicity to $Z = 0.005$. *Top*: maintaining the turbulence at a low level of $\delta = 10^{-5}$, the same as in the top left panel of Fig. 4, effectively quenches the formation of cold gas giants, while warm and hot gas giants can still form. The populations of sub-Neptunes, super-Earths, and rocky planets are relatively unaffected by the lower metallicity. *Bottom*: increasing the turbulence strength to $\delta = 3 \times 10^{-5}$ also quenches the formation of warm gas giants, with only a small population remaining in the 0.1–0.3 AU region.

Fig. 8. Two models with high $\alpha = 0.02$ and high $Z = 0.02$, giving the same dust mass as in the nominal model, but with half the gas mass. This may represent either an initially higher metallicity or a gradual gas loss to disc winds. The lower migration rates make it possible to form Jupiter analogues both at $\delta = 3 \times 10^{-5}$ (*top*) and at $\delta = 10^{-4}$ (*bottom*).

of cold gas giants difficult. We go on to test the effect of the migration rate for the formation of gas giant planets. We maintain the disc size and total dust mass but half the amount of gas in the disc, as could be the consequence of gas loss due to disc winds (Tabone et al. 2022; Zhao & Matsumura 2025). We mimic the effect of gas loss here by increasing the viscosity to $\alpha = 2 \times 10^{-2}$ while doubling the metallicity to $Z = 0.02$. We maintain the approximate initial planetesimal mass, despite the lower gas mass and hence lower Γ, by starting here at 40 times the characteristic mass formed by the streaming instability. Figure 8 shows the resulting populations for two values of the turbulence strength, $\delta = 3 \times 10^{-5}$ and $\delta = 10^{-4}$. Cold gas giants appear under both turbulence levels, which highlights the positive effect of gas removal for parking migrating planets in cold orbits. This overall demonstrates that even with rapid pebble accretion in the outer disc, reducing the migration rate of protoplanets leads to a better agreement with the population of cold gas giants.

6. Mapping the conditions for streaming instability and pebble accretion

We finally in this section map the conditions in the protoplanetary disc that allow planetesimal formation by the streaming instability in terms of Stokes number St and turbulence strength δ, as well as the outcome of pebble accretion calculations starting from 20 times the characteristic mass of planetesimals formed by the streaming instability.

6.1. Streaming instability and turbulence

We base the criterion for filament formation by the streaming instability on the threshold derived in Li & Youdin (2021) in terms of the mid-plane dust-to-gas ratio ϵ_0. This dust-to-gas ratio is then converted to a critical turbulence strength δ_c, above which the critical mid-plane density cannot be reached due to turbulence inhibiting pebble sedimentation, by inverting the equation

$$\epsilon_0 = Z\sqrt{\frac{\mathrm{St}+\delta_\mathrm{c}}{\delta_\mathrm{c}}}, \tag{16}$$

to yield $\delta_\mathrm{c}(\mathrm{St}, \epsilon_0(\mathrm{St}))$ for a given Stokes number. Here, Z is the ratio of the surface density of pebbles relative to the surface density of the gas (i.e. the metallicity). We take this approach rather than basing the metallicity threshold on simulations with forced turbulence (Lim et al. 2024), since simulations of weak turbulence caused by the magnetorotational instability show a mid-plane density threshold that is very similar to the non-turbulent case (Eriksson et al. 2026). We also ignore the possibility that turbulence excited by a physical instability could produce pressure bumps as a side effect, which can aid the streaming instability by concentrating pebbles towards the pressure maximum (Johansen et al. 2007, 2009a; Yang et al. 2018; Zhao et al. 2025; Eriksson et al. 2026).

The vertical shear instability, which is a plausible source of turbulence in protoplanetary discs (Nelson et al. 2013), has been demonstrated to allow the co-existence of a thin sedimented mid-plane layer of pebbles, where the streaming instability drives weak turbulence, together with significant large-scale vertical motion of the gas above and below the mid-plane (Schäfer & Johansen 2022; Huang & Bai 2025), effectively decoupling the weak turbulence experienced by the pebbles in the mid-plane from the stronger turbulence experienced by the bulk of the gas. Even when the vertical shear instability is given a head start to evolve before the streaming instability, the vertical shear instability exerts a scale-dependent diffusion on the dust, with the diffusion coefficient over the thickness of the pebble layer measured at the level of $\delta \sim 7\times10^{-5}$ (Schäfer et al. 2025). The sedimented pebbles are embedded in a large-scale up-down flow with a measured diffusion strength of $\delta \sim 4\times10^{-4}$ for pebbles with St = 0.03 and $Z = 0.02$ (Schäfer et al. 2025) as well as for pebbles with St = 0.1 and $Z = 0.01$ (Huang & Bai 2025). Pebbles in such a flow experience internal settling and low collision speeds driven by weak turbulence, while the pebble layer is forced to undulate around the mid-plane to a significant height dictated by the stronger large-scale turbulence (although the mid-plane layer height is significantly reduced by the drag-force exerted from the pebbles on the gas). The small-scale turbulent diffusion will thus dictate the fragmentation-limited growth of pebbles to proceed with a low value of δ, while the large-scale turbulent diffusion will dictate the pebble accretion rate through its determination over the mean mid-plane pebble density. The simulations of Schäfer et al. (2025) and Huang & Bai (2025) were nevertheless isothermal, which maximizes the strength of the vertical shear instability, and the effect of pebble back-reaction on the weaker turbulence that arises in simulations of the vertical shear instability with realistic cooling times (Pfeil et al. 2023) has currently not been probed.

We show the threshold metallicity for forming planetesimals by the streaming instability in Fig. 9, as a function of Stokes number ranging from St = 10^{-4} to St = 10^{-1}, for two values of the metallicity (Eq. (16)): $Z = 0.01$ and $Z = 0.02$ (the latter reflecting gas removal by disc winds or a local pile-up of pebbles, e.g. at the H_2O or CO ice lines, as discussed in Sect. 3). We overplot in Fig. 9 curves of constant relative mid-plane layer thickness $h = H_\mathrm{p}/H$, where H_p is the pebble scale-height and H is the gas scale-height, of $h = 0.01$, 0.05 and 0.1, due the direct observability of this physical quantity in protoplanetary discs (Pinte et al. 2016; Villenave et al. 2022), given knowledge of the gas scale-height from thermal modelling of observations of small dust grains in scattered light. We also indicate, with dot-dashed lines, the turbulent diffusion strength δ corresponding to a given Stokes number St for three values of the pebble fragmentation threshold speed, from Eq. (1), at either 1 AU (blue) or 50 AU (red).

The abrupt jump in the δ threshold around St ~ 0.01 in Fig. 9 is due to a transition in the metallicity threshold from less than unity to $\epsilon_0 \approx 2.5$ when decreasing the Stokes number below St = 0.01 (Carrera et al. 2015; Yang et al. 2017; Li & Youdin 2021); we note that this jump is not observed in simulations with imposed turbulence where the mid-plane density threshold at high St is significantly higher (Lim et al. 2024); however those simulations with imposed background turbulence only probed turbulence with strength down to $\delta = 10^{-4}$ and may not fully represent turbulence driven by a physical instability such as the vertical shear instability (Schäfer et al. 2025) or the magnetorotational instability (Eriksson et al. 2026).

6.2. Planetary systems

For three discrete values in each decade of St and δ, we also perform pebble accretion simulations starting from 20 times the characteristic mass of planetesimals formed by the streaming instability. We quantify the outcome of these simulations in terms of three symbolic circles in Fig. 9:

1. The yellow (left) circle marks the maximum mass of planets ending in orbits closer than 0.5 AU from the star;
2. The blue (middle) circle marks the maximum mass of planets ending in orbits between 0.5 and 1.5 AU, with a cap at $2\,M_\mathrm{E}$ to avoid temperate gas giant interlopers;
3. The red (right) circle marks the maximum mass of planets ending in orbits more distant than 3 AU.

The three circles thus represent (1) planets in hot and warm orbits (hot/warm gas giants, hot/warm sub-Neptunes and hot/warm super-Earths), (2) rocky planets in temperate Earth-like orbits, and (3) planets in cold orbits. For each category, we define a success criterion and mark the successful cases with a thick circle edge. For the yellow class, the success criterion is to form super-Earths and/or sub-Neptunes with the threshold mass set at $M = 1\,M_\mathrm{E}$, which we take as the dividing line between rocky planets, of lower masses, and super-Earths and sub-Neptunes. For the blue class, we take as success criterion to reach a mass of at least $M = 0.4\,M_\mathrm{E}$, which demarcates significant growth of rocky planets by pebble accretion. Finally, for the red class we adopt a success criterion of reaching a mass of $M = 100\,M_\mathrm{E}$, which is roughly the mass of Saturn. We emphasize that the inner and middle planet classes are likely to undergo substantial collisional evolution during and after the protoplanetary disc phase (Lambrechts et al. 2019) and that cold gas giants may be scattered into hot and warm orbits; both these effects are ignored here.

The top panel of Fig. 9 shows the results of the pebble accretion calculations with a large initial disc size of $R_1 = 112$ AU. Here, the formation of cold gas giants is possible up to a turbulence range between $\delta = 3\times10^{-5}$ and $\delta = 10^{-4}$ – and that requires Stokes numbers in the optimum range between St = 0.01 and St = 0.03. Pebbles of higher Stokes number drift towards the star too rapidly, so that there is insufficient time to grow cold gas giant planets before the disc has been drained of its pebbles. As St is decreased, so is the critical turbulence strength, with the threshold value to form cold gas giants reaching an ultra low value of $\delta = 10^{-6}$ for St = 0.001. The formation of super-Earths and sub-Neptunes has less strict

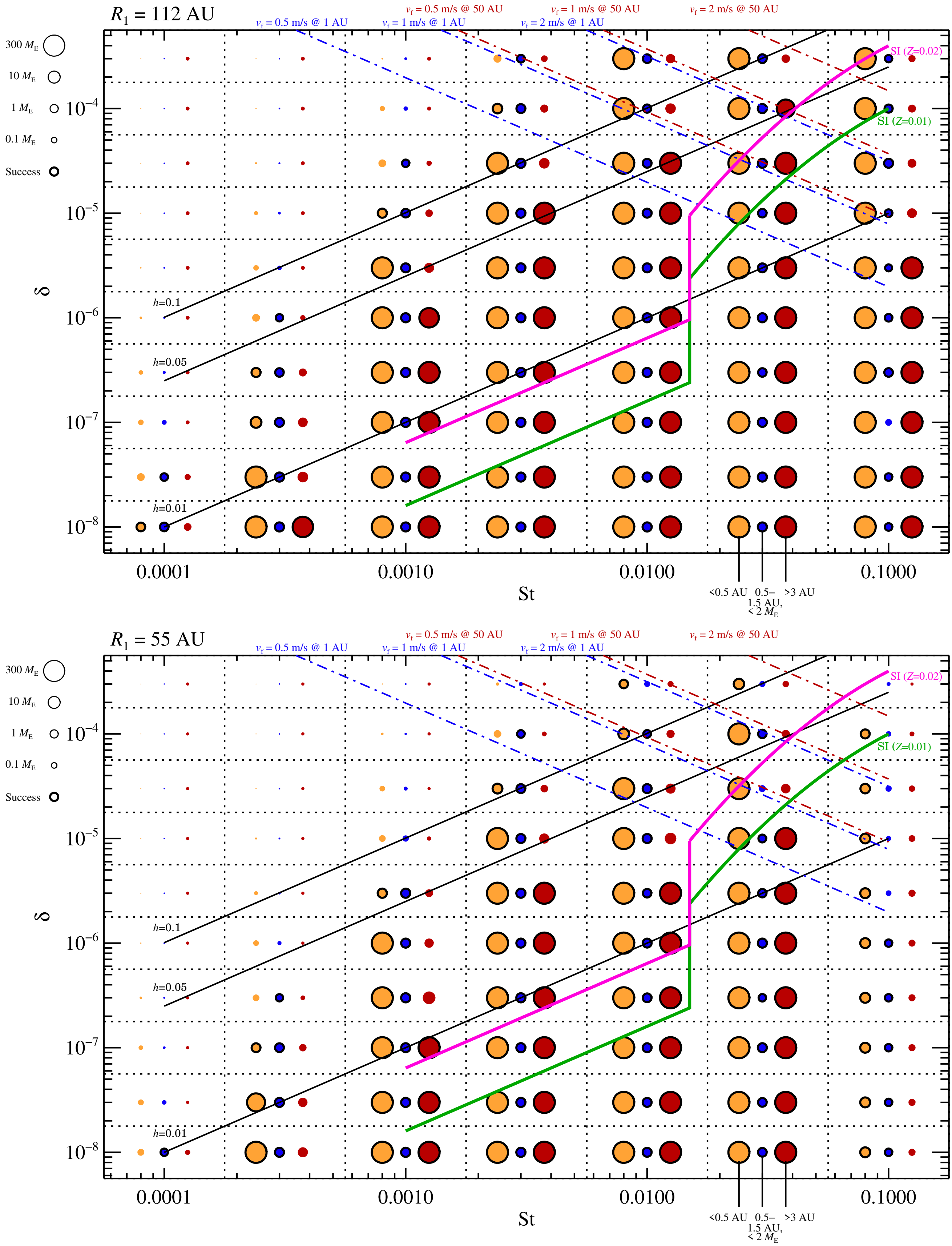

Fig. 9. Map of conditions for triggering planetesimal formation by the streaming instability as well as the outcome of planet formation simulations, both as a function of Stokes number St and turbulent diffusion coefficient δ. We use here a viscosity parameter for angular momentum transport of $\alpha = 10^{-2}$ and an initial disc of either 112 AU (*top*) or 55 AU (*bottom*). We refer to the main text for a full discussion of these two plots.

requirements on the turbulence strengths than the formation of cold gas giants, with a relatively high turbulence strength of (at least) $\delta = 3 \times 10^{-4}$ allowed for optimum spot range in Stokes number (between St = 0.01 and St = 0.03). Temperate rocky planets follow super-Earths quite closely in how the limiting turbulence strength depends on the Stokes number, although three times higher turbulence levels are allowed for forming rocky planet embryos at St = 0.003 and St = 0.001 relative to the threshold for super-Earth formation.

The lower panel of Fig. 9 maps the results when using a more nominal initial protoplanetary disc size of $R_1 = 55\,\mathrm{AU}$. The formation of cold gas giants now requires that the turbulence strength is at most $\delta = 10^{-5}$ at an optimal value of St = 0.03. The threshold for super-Earth formation remains within the strength of turbulence measured for the vertical shear instability ($\delta = 3 \times 10^{-4}$) for St = 0.01 to St = 0.03. These reasonable formation parameters for super-Earths within a protoplanetary with a nominal initial size are in agreement with the approximately 50% occurrence rate of planets with radii between one and four times the radius of Earth in hot and warm orbits around solar-type stars (Marcy et al. 2014). The threshold for super-Earth formation falls by a factor of three compared to the larger disc for St $\leq$ 0.003. The formation of substantial rocky planet embryos requires $\delta \leq 10^{-4}$ in the smaller disc, due to the faster draining of the pebble flux and hence enhanced migration compared to the larger disc.

7. Summary

In this paper, we have explored how planetesimal formation by the streaming instability and planetary growth by pebble accretion depend on the turbulence strength, pebble Stokes number, and initial disc size. We summarize here a number of salient points raised by our study.

Pebble accretion can operate directly on the most massive planetesimals formed by the streaming instability. We demonstrated analytically that the characteristic mass of planetesimals formed by the streaming instability is approximately one-tenth of the threshold mass above which pebble accretion becomes efficient, if planetesimals form at the early stages of protoplanetary disc evolution with a Stokes number of order St $\sim 10^{-2}$. We also showed that the characteristic planetesimal mass and the pebble accretion threshold mass scale similarly with many properties of the protoplanetary disc, so that these dependences cancel out when considering their ratio, with the exception of the Stokes number (which to first order does not seem to affect the characteristic mass of the planetesimals) and the self-gravity parameter Γ (which does not affect the onset of pebble accretion). The resemblance of the characteristic mass of planetesimals formed by the streaming instability and the pebble accretion threshold mass implies that pebble accretion can operate efficiently already on planetesimals that are born at the upper, exponential end of the initial mass function (Schäfer et al. 2017, 2024). The initial mass function of planetesimals formed by the streaming instability is nevertheless not completely understood. Particularly, the masses of the largest bodies could be underestimated due to limited simulation domains (Schäfer et al. 2024) or overestimated due to artificial merging of clumps at low resolution (Johansen et al. 2015; Simon et al. 2016). We also ignored an early, rapid growth phase by pebble accretion within the dense pebble mid-plane layer that may boost the masses of the largest planetesimals to values well above their initial birth masses. We also emphasize that while giant impacts are likely too rare in the outer disc to assist pebble accretion in forming the cores of cold gas giants (Lorek & Lambrechts 2026), accretion of planetesimals and protoplanets is expected to be a major contributor to planetary growth in the inner disc, even though pebble accretion operates well there already on the planetesimal birth sizes.

Migration matters for cold gas giants. The formation of a cold gas giant similar to Jupiter requires both weak turbulence ($\delta \lesssim 10^{-4}$) and a very large disc size ($R_1 \gtrsim 100\,\mathrm{AU}$). These tough requirements on the formation of cold gas giants found here may shed light on why this class of planets is relatively rare at solar metallicity (Fulton et al. 2021): their formation is only possible within the ~10% largest and most massive protoplanetary discs. We nevertheless demonstrated that reducing the amount of gas in the disc while maintaining the amount of dust leads to colder final orbits of the outermost gas giant planets. Removal of moderate amounts of gas by disc winds could thus be key to preventing gas giants from migrating to the terrestrial planet zone (Zhao & Matsumura 2025). The speed of Type I migration could also be reduced by considering more sources of positive torques from the gas onto the growing protoplanet, not included here, such as the dynamical corotation torque (Ndugu et al. 2021; Savvidou & Bitsch 2023). We also ignored pressure bumps in the disc in order to study the limits to planet formation unaided by disc substructures. Pressure bumps nevertheless do appear naturally in simulations of MHD turbulence in the outer disc regulated by ambipolar diffusion (Béthune et al. 2016; Xu & Bai 2022; Eriksson et al. 2026) and in the inner disc regulated by the Hall effect (Krapp et al. 2018), by viscosity transitions in the disc, (Lyra et al. 2008b; Chatterjee & Tan 2014), by streamer infall (Zhao et al. 2025), and by planet torques (Lyra et al. 2009; Lau et al. 2024). The increased pebble density in a pressure bump can significantly boost the growth rate of distant cores, and can thus move the final planet more easily into cold or even ultra-cold orbits (Jiang & Ormel 2023).

Ice giants are hard to form even with pebble accretion. Ice giants similar to Uranus and Neptune in very cold orbits are even harder to form than cold gas giants under all the conditions explored here (as also concluded by Eriksson et al. 2023), but the Solar System's two ice giants likely migrated outwards by scattering planetesimals after the dissipation of the protoplanetary disc (Fernandez & Ip 1984; Malhotra 1993) and could therefore have formed further in where pebble accretion rates are higher. Forming ice giants in the 15–20 AU region may nevertheless still require a gas-depleted disc to reduce their migration path.

Super-Earths and sub-Neptunes form under a wide range of conditions. These types of planets occur around approximately 50% of solar-type stars (Marcy et al. 2014) and planet formation theory should therefore be able to form them straightforwardly under nominal protoplanetary disc conditions. We show that super-Earths and sub-Neptunes form in both large and mid-sized protoplanetary discs and that they tolerate a turbulence level similar to that measured for the vertical shear instability ($\delta \sim 3 \times 10^{-4}$, Schäfer et al. 2025; Huang & Bai 2025). More simulations will be required in the future – under turbulence driven by both the vertical shear instability with realistic gas cooling times set by the dust size distribution (Pfeil et al. 2023) and by the magnetorotational instability under the influence of Hall diffusion, Ohmic diffusion, and ambipolar diffusion – in order to understand how various realistic sources of gas turbulence interacting with the streaming instability affect pebble dynamics, and thus pebble accretion rates of super-Earths and sub-Neptunes growing in the inner disc.

Wet rocky planet embryos emerge readily around the water ice line. In this study we distinguished the parameter for angular momentum transport (α) from the parameter characterizing the turbulence level in the disc (δ), motivated by disc wind models that demonstrate cold accretion through the inner disc driven by discs winds (Mori et al. 2019, 2021). The water ice line is therefore well within 1 AU for most the lifetime of the protoplanetary disc, when the turbulence level is weak. Planets that grow just outside of the water ice line nevertheless sublimate the icy mantles from their accreted pebbles once these planets reach masses above 1% of an Earth mass (Johansen et al. 2021). Our rocky planet embryos growing around 1 AU are therefore endowed with water mass fractions at the level of ~0.1%–1%, which is similar to estimates of the Earth's water budget including a majority of water residing in the core (Li et al. 2020). Our water estimates nevertheless do not take into account destruction of water by reaction with Fe or Si (Johansen et al. 2023a; Werlen et al. 2025). We also ignored protoplanet and planet collisions that are highly likely to occur in the inner 10 AU both during and after the gas disc phase (Lambrechts et al. 2019); we therefore clearly underestimate planetary growth as well as water budgets for the planets that form in the inner disc. Future N-body simulations can be used straightforwardly to include collisions while tracking the water composition, but at the cost of much higher computation times and more stochasticity in the results that will require running multiple random initial conditions for each disc model (Bitsch et al. 2019; Izidoro et al. 2021; Yzer et al. 2025).

Future progress on understanding the formation of planetary systems will also benefit from better observational constraints on initial protoplanetary disc masses and radii (e.g. Ohashi et al. 2023) as well as their temporal evolution (e.g. Tychoniec et al. 2020; Zamudio-Ruvalcaba et al. 2025). Future facilities such as SKA (Ilee et al. 2020), ngVLA (Ricci et al. 2018), and an extended ALMA (Burrill et al. 2022) will also be key to probing conditions in the inner regions of protoplanetary discs, such as detecting substructures caused by forming super-Earths there, measuring the sizes and Stokes numbers of inner-disc pebbles, as well as putting constraints on turbulence levels in the disc regions where the vertical shear instability is expected to be active in concert with the streaming instability.

Acknowledgements. We thank the anonymous referee for insightful comments that helped improve the manuscript. A.J. acknowledges funding from the Carlsberg Foundation (Semper Ardens: Advance grant FIRSTATMO). W.L. acknowledges funding from NASA Emerging Worlds program via grant No. 80NSSC22K1419 and NSF via grant 2511672. W.L. further acknowledges the hospitality of the Center for Star and Planet Formation at the University of Copenhagen during a sabbatical leave, which facilitated discussions that contributed to this paper.

References

Appelgren, J., Lambrechts, M., & van der Marel, N. 2023, A&A, 673, A139
Arakawa, S., Okuzumi, S., Tatsuuma, M., et al. 2023, ApJ, 951, L16
Bai, X.-N., & Stone, J. M. 2010, ApJ, 722, 1437
Baraffe, I., Homeier, D., Allard, F., et al. 2015, A&A, 577, A42
Bate, M. R. 2018, MNRAS, 475, 5618
Batygin, K., & Morbidelli, A. 2022, A&A, 666, A19
Baumann, T., & Bitsch, B. 2020, A&A, 637, A11
Benítez-Llambay, P., Masset, F., Koenigsberger, G., et al. 2015, Nature, 520, 63
Benítez-Llambay, P., & Pessah, M. E. 2018, ApJ, 855, L28
Béthune, W., Lesur, G., & Ferreira, J. 2016, A&A, 589, A87
Béthune, W., Lesur, G., & Ferreira, J. 2017, A&A, 600, A75
Birnstiel, T., Ormel, C. W., & Dullemond, C. P. 2011, A&A, 525, A11
Bitsch, B., Johansen, A., Lambrechts, M., et al. 2015, A&A, 575, A28
Bitsch, B., Morbidelli, A., Johansen, A., et al. 2018, A&A, 612, A30
Bitsch, B., Izidoro, A., Johansen, A., et al. 2019, A&A, 623, A88
Blum, J., & Wurm, G. 2000, Icarus, 143, 138
Bosman, A. D., Appelgren, J., Bergin, E. A., et al. 2023, ApJ, 944, L53
Bottke, W. F., Durda, D. D., Nesvorný, D., et al. 2005, Icarus, 175, 111
Brauer, F., Dullemond, C. P., & Henning, T. 2008, A&A, 480, 859
Buchhave, L., Latham, D., Johansen, A., et al. 2012, Nature, 486, 375
Burrill, B. P., Ricci, L., Harter, S. K., et al. 2022, ApJ, 928, 40
Carrera, D., Johansen, A., & Davies, M. B. 2015, A&A, 579, A43
Carrera, D., Gorti, U., Johansen, A., et al. 2017, ApJ, 839, 16
Chambers, J. 2018, ApJ, 865, 30
Chambers, J. 2019, ApJ, 879, 2, 98
Chambers, J. E., & Wetherill, G. W. 1998, Icarus, 136, 304
Chatterjee, S., & Tan, J. C. 2014, ApJ, 780, 53
Chen, D.-C., Mordasini, C., Emsenhuber, A., et al. 2025, A&A, 701, A94
Danti, C., Lambrechts, M., & Lorek, S. 2025, A&A, 700, A132
Desch, S. J., & Turner, N. J. 2015, ApJ, 811, 156
Dominik, C., & Dullemond, C. P. 2024, A&A, 682, A144
Drążkowska, J., & Alibert, Y. 2017, A&A, 608, A92
Dullemond, C. P., & Dominik, C. 2005, A&A, 434, 971
Eriksson, L. E. J., Mol Lous, M. A. S., Shibata, S., et al. 2023, MNRAS, 526, 4860
Eriksson, L. E. J., Xu, Z., Lim, J., et al. 2026, A&A, submitted [arXiv:2603.17195]
Fernandez, J. A., & Ip, W.-H. 1984, Icarus, 58, 109
Fortier, A., Alibert, Y., Carron, F., et al. 2013, A&A, 549, A44
Fritscher, M., & Teiser, J. 2021, ApJ, 923, 134
Fulton, B. J., Rosenthal, L. J., Hirsch, L. A., et al. 2021, ApJS, 255, 14
Gundlach, B., & Blum, J. 2015, ApJ, 798, 34
Gundlach, B., Schmidt, K. P., Kreuzig, C., et al. 2018, MNRAS, 479, 1273
Gurrutxaga, N., Johansen, A., Lambrechts, M., et al. 2024, A&A, 682, A43
Güttler, C., Blum, J., Zsom, A., et al. 2010, A&A, 513, A56
Hartmann, L., Calvet, N., Gullbring, E., et al. 1998, ApJ, 495, 385
Huang, P., & Bai, X.-N. 2025, ApJ, 986, L13
Ida, S., & Guillot, T. 2016, A&A, 596, L3
Ida, S., Guillot, T., & Morbidelli, A. 2016, A&A, 591, A72
Ida, S., Tanaka, H., Johansen, A., et al. 2018, ApJ, 864, 77
Ilee, J. D., Hall, C., Walsh, C., et al. 2020, MNRAS, 498, 5116
Izidoro, A., Bitsch, B., Raymond, S. N., et al. 2021, A&A, 650, A152
Jiang, H., & Ormel, C. W. 2023, MNRAS, 518, 3877
Jiang, H., Macías, E., Guerra-Alvarado, O. M., et al. 2024, A&A, 682, A32
Jiang, H., Long, F., Macías, E., et al. 2025, ApJ, 993, 166
Johansen, A., & Bitsch, B. 2019, A&A, 631, A70
Johansen, A., & Lambrechts, M. 2017, Annu. Rev. Earth Planet. Sci., 45, 359
Johansen, A., & Lacerda, P. 2010, MNRAS, 404, 475
Johansen, A., & Youdin, A. 2007, ApJ, 662, 627
Johansen, A., Oishi, J. S., Mac Low, M.-M., et al. 2007, Nature, 448, 1022
Johansen, A., Youdin, A., & Klahr, H. 2009a, ApJ, 697, 1269
Johansen, A., Youdin, A., & Mac Low, M.-M. 2009b, ApJ, 704, L75
Johansen, A., Mac Low, M.-M., Lacerda, P., et al. 2015, Sci. Adv., 1, 1500109
Johansen, A., Ida, S., & Brasser, R. 2019, A&A, 622, A202
Johansen, A., Ronnet, T., Bizzarro, M., et al. 2021, Sci. Adv., 7, eabc0444
Johansen, A., Ronnet, T., Schiller, M., et al. 2023a, A&A, 671, A74
Johansen, A., Ronnet, T., Schiller, M., et al. 2023b, A&A, 671, A75
Johansen, A., Bannister, M. T., Dones, L., et al. 2025, Centaurs, 2
Kaufmann, N., Guilera, O. M., Alibert, Y., et al. 2025, A&A, 696, A65
Kimura, H., Wada, K., Senshu, H., et al. 2015, ApJ, 812, 67
Klahr, H., & Schreiber, A. 2021, ApJ, 911, 9
Kokubo, E., & Ida, S. 2000, Icarus, 143, 15
Kokubo, E., & Ida, S. 2007, ApJ, 671, 2082
Krapp, L., Gressel, O., Benítez-Llambay, P., et al. 2018, ApJ, 865, 105
Lambrechts, M., & Johansen, A. 2012, A&A, 544, A32
Lambrechts, M., & Johansen, A. 2014, A&A, 572, A107
Lambrechts, M., Morbidelli, A., Jacobson, S. A., et al. 2019, A&A, 627, A83
Lau, T. C. H., Birnstiel, T., Drążkowska, J., et al. 2024, A&A, 688, A22
Levison, H. F., Thommes, E., & Duncan, M. J. 2010, AJ, 139, 1297
Levison, H. F., Kretke, K. A., Walsh, K. J., et al. 2015, PNAS, 112, 14180
Li, R., & Chiang, E. 2025, ApJ, 995, 214
Li, R., & Youdin, A. N. 2021, ApJ, 919, 107
Li, Y., Vočadlo, L., Sun, T., et al. 2020, Nat. Geosci., 13, 453
Lim, J., Simon, J. B., Li, R., et al. 2024, ApJ, 969, 130
Liu, B., Ormel, C. W., & Johansen, A. 2019a, A&A, 624, A114
Liu, B., Lambrechts, M., Johansen, A., et al. 2019b, A&A, 632, A7
Liu, B., Lambrechts, M., Johansen, A., et al. 2020, A&A, 638, A88
Liu, B., Johansen, A., Lambrechts, M., et al. 2022, Sci. Adv., 8, eabm3045

Lodders, K. 2003, ApJ, 591, 1220
Lorek, S., & Johansen, A. 2022, A&A, 666, A108
Lorek, S., & Lambrechts, M. 2026, A&A, 707, A244
Lyra, W., Johansen, A., Klahr, H., et al. 2008a, A&A, 479, 883
Lyra, W., Johansen, A., Klahr, H., et al. 2008b, A&A, 491, L41
Lyra, W., Johansen, A., Klahr, H., et al. 2009, A&A, 493, 1125
Lyra, W., Johansen, A., Cañas, M. H., et al. 2023, ApJ, 946, 60
Malhotra, R. 1993, Nature, 365, 819
Marcy, G. W., Weiss, L. M., Petigura, E. A., et al. 2014, PNAS, 111, 12655
Mori, S., Bai, X.-N., & Okuzumi, S. 2019, ApJ, 872, 98
Mori, S., Okuzumi, S., Kunitomo, M., et al. 2021, ApJ, 916, 72
Musiolik, G., Teiser, J., Jankowski, T., et al. 2016, ApJ, 818, 16
Musiolik, G., & Wurm, G. 2019, ApJ, 873, 58
Najita, J. R., & Bergin, E. A. 2018, ApJ, 864, 168
Ndugu, N., Bitsch, B., Morbidelli, A., et al. 2021, MNRAS, 501, 2017
Nelson, R. P., Gressel, O., & Umurhan, O. M. 2013, MNRAS, 435, 2610
Nielsen, J., Gent, M. R., Bergemann, M., Eitner, P., & Johansen, A. 2023, A&A, 678, A74
Nielsen, J., Johansen, A., Bali, K., et al. 2025, A&A, 695, A184
Ohashi, N., Tobin, J. J., Jørgensen, J. K., et al. 2023, ApJ, 951, 8
Okuzumi, S., Tanaka, H., Kobayashi, H., et al. 2012, ApJ, 752, 106
Ormel, C. W. 2017, Formation Evolution, and Dynamics of Young Solar Systems, 445, 197
Ormel, C. W., & Klahr, H. H. 2010, A&A, 520, A43
Paardekooper, S.-J. 2014, MNRAS, 444, 2031
Paardekooper, S.-J., Baruteau, C., Crida, A., et al. 2010, MNRAS, 401, 1950
Paardekooper, S.-J., Baruteau, C., & Kley, W. 2011, MNRAS, 410, 293
Pfeil, T., Birnstiel, T., & Klahr, H. 2023, ApJ, 959, 121
Pinte, C., Dent, W. R. F., Ménard, F., et al. 2016, ApJ, 816, 25
Piso, A.-M. A., & Youdin, A. N. 2014, ApJ, 786, 1, 21
Qian, Y., & Wu, Y. 2025, ApJ, 995, 115
Raymond, S. N., Quinn, T., & Lunine, J. I. 2004, Icarus, 168, 1
Ricci, L., Liu, S.-F., Isella, A., et al. 2018, ApJ, 853, 110
Ros, K., & Johansen, A. 2013, A&A, 552, A137
Ros, K., & Johansen, A. 2024, A&A, 686, A237
Safronov, V. S. 1969, Evoliutsiia doplanetnogo oblaka
Savvidou, S., & Bitsch, B. 2023, A&A, 679, A42
Schäfer, U., & Johansen, A. 2022, A&A, 666, A98
Schäfer, U., Yang, C.-C., & Johansen, A. 2017, A&A, 597, A69
Schäfer, U., Johansen, A., Haugbølle, T., et al. 2024, A&A, 691, A258
Schäfer, U., Johansen, A., & Flock, M. 2025, A&A, 694, A57
Schneider, A. D., & Bitsch, B. 2021, A&A, 654, A71
Schoonenberg, D., & Ormel, C. W. 2017, A&A, 602, A21
Simon, J. B., Armitage, P. J., Li, R., et al. 2016, ApJ, 822, 55
Stammler, S. M., Birnstiel, T., Panić, O., et al. 2017, A&A, 600, A140
Tabone, B., Rosotti, G. P., Cridland, A. J., et al. 2022, MNRAS, 512, 2290
Testi, L., Natta, A., Shepherd, D. S., et al. 2003, A&A, 403, 323
Thommes, E. W., Duncan, M. J., & Levison, H. F. 2003, Icarus, 161, 431
Tobin, J. J., & Sheehan, P. D. 2024, ARA&A, 62, 203
Tong, S., Alexander, R., & Rosotti, G. 2026, MNRAS, 545, 4
Tychoniec, Ł., Manara, C. F., Rosotti, G. P., et al. 2020, A&A, 640, A19
Ueda, T., Andrews, S. M., Carrasco-González, C., et al. 2025, ApJ, 990, 183
Villenave, M., Stapelfeldt, K. R., Duchêne, G., et al. 2022, ApJ, 930, 11
Villenave, M., Podio, L., Duchêne, G., et al. 2023, ApJ, 946, 70
Villenave, M., Rosotti, G. P., Lambrechts, M., et al. 2025, A&A, 697, A64
Wang, Y., Ormel, C. W., Huang, P., et al. 2023, MNRAS, 523, 6186
Werlen, A., Dorn, C., Burn, R., et al. 2025, ApJ, 991, L16
Wilner, D. J., D'Alessio, P., Calvet, N., et al. 2005, ApJ, 626, L109
Xu, Z., & Bai, X.-N. 2022, ApJ, 924, 3
Yang, C.-C., Johansen, A., & Carrera, D. 2017, A&A, 606, A80
Yang, C.-C., Mac Low, M.-M., & Johansen, A. 2018, ApJ, 868, 27
Yap, T. E., & Batygin, K. 2024, Icarus, 417, 116085
Youdin, A. N., & Goodman, J. 2005, ApJ, 620, 459
Youdin, A., & Johansen, A. 2007, ApJ, 662, 613
Yun, H.-G., Kim, W.-T., Bae, J., et al. 2022, ApJ, 938, 102
Yzer, M., Brasser, R., & ten Kate, I. L. 2025, A&A, 698, A307
Zamudio-Ruvalcaba, L. F., Espaillat, C. C., Ribas, Á., et al. 2025, ApJ, 995, 16
Zhao, Y., & Matsumura, S. 2025, A&A, 693, A280
Zhao, H., Lau, T. C. H., Birnstiel, T., et al. 2025, A&A, 694, A205
Zsom, A., Ormel, C. W., Güttler, C., et al. 2010, A&A, 513, A57